SOLPS-ITER simulations of a CPS-based liquid metal divertor for the EU DEMO: Li vs. Sn

G. F. Nallo[a*], G. Mazzitelli[b], M. Moscheni[a], F. Subba[a], R. Zanino[a]

[a] *NEMO group, Dipartimento Energia, Politecnico di Torino, Torino, Italy*
[b] *ENEA, Fusion and Technologies for Nuclear Safety Department, C.R.Frascati,C.P.65-00044Frascati,Rome,Italy*

[*]Corresponding author

Abstract

In this work, we study the effect of installing a liquid metal divertor (LMD) using a capillary-porous structure in the EU DEMO tokamak within the same envelope of the baseline solid divertor. We used the SOLPS-ITER code to model the Scrape-Off Layer (SOL) plasma and neutrals, coupled to a target thermal model to enable the self-consistent calculation of the LM target erosion rate, and adopting a fluid neutral model for the sake of simplicity.

First calculations considering only D and Li (or Sn) showed a significant reduction of the steady state target heat load with respect to simulations considering only D, thanks to *vapor shielding*. Nevertheless, the computed peak target heat flux (~31 MW/m^2 and ~44 MW/m^2 for Li and Sn, respectively) was still larger than/borderline to the power handling limit of the LMD concepts considered. Moreover, the impurity concentration in the pedestal - a proxy for the core plasma dilution/contamination - was computed to be ~9% and ~0.02%, respectively, i.e. above/close to tolerability limits suggested by previous COREDIV calculations. These results indicate that the operational window of an LMD for the EU DEMO, without any additional impurity seeding, might be too narrow, if it exists, and that Sn looks more promising than Li.

A second set of calculations was then performed simulating Ar seeding in the SOL, to further reduce the target heat load, and consequently the metal erosion rate. It was found that the mitigation of the plasma heat load due to Ar radiation in the SOL effectively replaces the radiation associated to vapor shielding in front of the target, thus allowing to operate the LMD in a regime of low target erosion. The resulting operational window was found to be significantly wider, both in terms of tolerable peak target heat flux and of acceptable core plasma contamination.

Keywords: Nuclear fusion reactors, Tokamak, Power Exhaust, Liquid Metal Divertor, SOLPS-ITER

1. Introduction and motivation

The identification of a strategy to solve the Power Exhaust (PEX) problem in future fusion devices is among the milestones indicated in the recently updated European Research Roadmap to the Realisation of Fusion Energy [1]. The baseline approach currently being considered for the EU DEMO reactor consists in using actively cooled W monoblocks as divertor targets, while relying on seeded impurities (e.g. Ar) to dissipate via isotropic radiation a significant fraction (~90% [2,3]) of the power crossing the separatrix, which is otherwise anisotropically advected/conducted by the plasma to the divertor itself. Alongside with the refinement of this approach, alternative solutions are being investigated, including Liquid Metal Divertors (LMDs) [4,5]. Among the proposed LMD concepts, the one adopting an LM-filled CPS as the plasma-facing surface (PFS) is currently considered to be the most mature [4]. The effectiveness of capillary forces in preventing LM droplet ejection and splashing phenomena, as well as the capability of this concept to withstand large plasma heat fluxes (of several tens of MW/m^2), have indeed been demonstrated experimentally both in tokamaks and in linear plasma devices [6–9]. The most attractive feature of a CPS-based LMD is its self-healing nature: the PFS is indeed passively replenished by capillary forces, thus compensating for the relatively large erosion rate of an LM target, which is caused by both sputtering and evaporation. Moreover, the eroded metal is responsible for the *vapor shielding* effect, i.e. the isotropic radiation of part of the plasma power in the proximity of the target, leading to a beneficial self-regulation of the target heat load and, consequently, of the erosion rate [10,11]. These features, together with the absence of thermo-mechanical stresses at the interface between the CPS and the solid substrate [12], have the potential to guarantee a longer divertor lifetime and a superior resilience to transient events with respect to the current baseline solution [13].

Li and Sn are currently regarded as the most promising candidates for an LMD [4]. For a given plasma heat and particle flux impinging on the target, a larger mass flux is eroded from a Li target with respect to a Sn target, due to the larger sputtering yield and vapour pressure. Conversely, for a given amount of eroded metal, Sn leads to larger plasma cooling, mostly associated to line radiation [14]. For both Li and Sn, the *vapor shielding* effect has been experimentally observed [15,16]. However, this self-mitigation of the target heat load might still fail to prevent an excessive erosion rate, leading to unacceptable core plasma dilution (in the case of Li) or to intolerable radiative energy losses in the core plasma (in the case of Sn) [2]. Moreover, albeit partially self-mitigated, the peak target heat flux might still overcome the power handling capability of the CPS-based LMD target, which is limited by e.g. the maximum tolerable thermo-mechanical stresses on the solid substrate supporting the CPS [17], the Critical Heat Flux (CHF) to the coolant [18], or the maximum PFS replenishment rate allowed by the CPS [19]. Therefore, the strategy of seeding external impurities such as Ar to increase

---

author's email: giuseppefrancesco.nallo@polito.it

the SOL plasma radiation and, consequently, further mitigate the target heat load – a strategy that is strictly necessary for a conventional solid divertor – may be considered also for an LMD [20].

Modelling the Scrape-Off Layer (SOL) plasma in the presence of an LMD is essential to predict whether an operating window for this system exists, both in terms of core plasma compatibility and of target heat load. This challenge has been addressed in the past by means of simplified models in [14,21–23]. Recently, more detailed simulations, including the transport of the eroded metal in the SOL and a detailed account of its interactions with the plasma, have been performed by means of 2D edge plasma codes. Notably, the UEDGE, SOLPS 4.3 and SOLPS-ITER codes were used to study a Li vapor box divertor for the FSNF facility, the T-15MD tokamak and the NSTX-U tokamak, respectively [24–26]. The TECXY code was used to study a CPS-based LMD for both the EU DEMO and the DTT [27,28], also including a 1D thermal model of the LM target to self-consistently account for target evaporation. First integrated target-edge-core simulations for the EU DEMO with an LMD were also performed using COREDIV [29].

In the present work, the SOLPS-ITER code is used, for the first time, to simulate the edge plasma of the EU DEMO equipped with a CPS-based LMD, comparing Li and Sn as LMs. The target response is considered self-consistently by coupling SOLPS-ITER to a thermal model to determine the surface temperature distribution, in order to correctly describe the feedback on the SOL plasma. This approach enables to present a fair comparison of Li and Sn as target materials, in terms of target heat flux and erosion. The effect of the eroded metal on the core plasma dilution/contamination is also studied, although it is noticed that a detailed evaluation of the impurity accumulation in the core plasma would require coupling SOLPS-ITER to a core transport code, which is beyond the scope of the present study. The effectiveness of Ar seeding in reducing the surface heat flux and erosion rate is also assessed. Finally, a methodology to account for the possibly non negligible radiative heat load on the LM target is proposed.

This paper is organized as follows: we shall first describe the system under study in section 2. The phenomenology of metal emission and the interactions with the plasma are then briefly recalled in section 3. The model and the simulation strategy are described in section 4. Results of simulations without and with Ar seeding are finally presented and discussed in sections 5.1 and 5.2, respectively, comparing the behavior of the LMD in the case of Li and in the case of Sn.

2. System description

2.1. Vessel shape and magnetic equilibrium

Here we use the same wall profile and magnetic equilibrium already adopted in [20], in which we replace the divertor target material (originally W) with Li (or Sn). The first wall profile is shown in Figure 1, together with the mesh. The implications of the simulation domain not extending up to the physical wall are discussed in section 4.1.

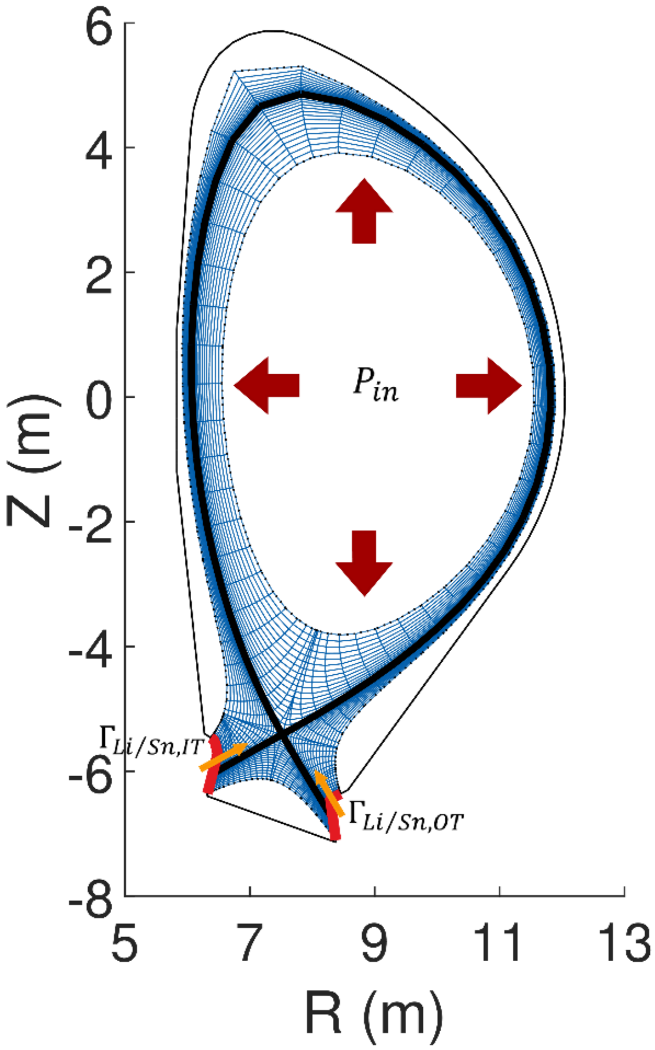

Figure 1. Sketch of the DEMO first wall geometry and mesh used for the simulations. The thick black line represents the separatrix and the red segments are the divertor targets. The power input in the domain (P_{in}), as well as the impurity emission from the inboard and outboard targets ($\Gamma_{Li/Sn,IT}$ and $\Gamma_{Li/Sn,OT}$, respectively) are also indicated.

2.2. LM target

For Li, the design proposed by Vertkov et al. in [17] is considered. This design, shown in Figure 2 (a), consists of a thin (2 mm) W plate covered by a Li-filled CPS, 0.5 mm thick. The cooling is achieved by means of a water-gas spray impinging on the back of the plate – the side not exposed to the plasma heat flux. This cooling strategy has been experimentally demonstrated to provide a heat transfer coefficient as large as 70-100 kW/m^2/K. The maximum tolerable heat flux of this design is ~20 MW/m^2, the limiting factor being the mechanical stresses on the actively cooled W substrate on which the plasma-facing CPS is placed [17].

For Sn, the design proposed by ENEA in [18] is instead considered. The cross-section of the plasma-facing unit of this design is reported in Figure 2 (b). For this design, a 2 mm-thick CPS, intended to continuously resupply the PFS with liquid Sn passively pumped from an LM reservoir, is placed on top of a CuCrZr heat sink, which is actively cooled by pressurized water (50 bar) flowing in cooling channels. For this design, a heat flux as large as ~40 MW/m^2 can be tolerated, the limiting factor being the CHF to the coolant [18].

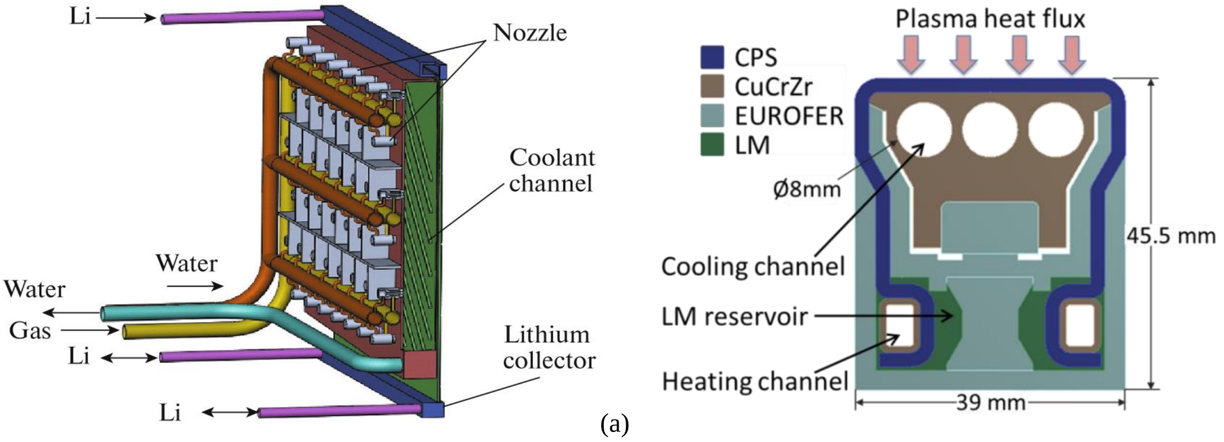

(a) (b)

Figure 2. Li CPS divertor, reproduced from [30] *with permission (left) and poloidal section of a single unit of the Sn CPS divertor considered for this study* [18] *(right).*

3. Phenomenology

The plasma heat and particle loads determine the erosion of the LM filling the CPS. One erosion mechanism, which is also present in the case of a solid divertor, is *physical sputtering*. It has been observed experimentally that, in the case of Li, ~2/3 of the total physically sputtered particles are ions, the rest being atoms [31]. Due to the sheath potential developing at the plasma-wall interface, sputtered ions can be assumed to be immediately redeposited onto the target, while atoms are emitted towards the plasma. On a liquid surface, two additional processes, *thermal sputtering* and *evaporation*, occur [32]. Thermal sputtering depends on the target surface temperature and plasma particle flux, while evaporation only depends on the target surface temperature. Note that erosion of the CPS material (typically W) can be neglected, based on the assumption that the CPS is always wetted by the LM.

The actual *net* erosion rate associated with the above-mentioned erosion mechanisms is lower than the theoretical *gross* erosion rate. For the scenario investigated in the present work, the most significant contribution to the difference is prompt (i.e., within one gyro-radius from the surface) neutral ionization and consequent redeposition on the target [33]. For the EU DEMO scenario here considered, as much as ~99% of the atoms can be promptly redeposited [34], depending on the target material and on the local plasma temperature and magnetic field. Another possible effect contributing to the suppression of the gross erosion is associated to D retention in the LM layer [32]. However, this effect is negligible for Sn [35] and also for Li, if the surface temperature is above 650 K [36]. For this reason, it will be neglected in the present work. This assumption also implies that the LMD operates in high recycling regime.

We will employ the following terminology throughout the paper for particles not promptly redeposited:

- the term *vapor* indicates metal atoms arising from target evaporation and sputtering;
- the term *fuel neutrals* indicates hydrogenic atoms arising from fuel recycling at the target.

Both vapor and fuel neutrals interact with the SOL plasma, undergoing ionization, recombination, excitation – with consequent line radiation – and/or charge-exchange. The actual metal charge state distribution depends on the local electron temperature and density, as well as on the interplay between friction, thermal forces, and radial diffusion. These plasma-vapor interactions are responsible for the above-mentioned *vapor shielding* effect [11,23,37], which contributes to lower the peak heat flux on the target, resulting in a self-regulation of the erosion rate. The latter reduces the vapor source, providing in turn a negative feedback on the shielding effect. To properly account for this phenomenology, the SOL plasma calculation was coupled to a model for the target erosion, see section 4.2, thereby allowing to compute the sputtering and evaporation rates consistently with the plasma heat load.

As a final remark, we note here that, depending on the net erosion rate, it could be necessary to design a strategy to recollect the vapor condensed on the FW, to avoid undesired accumulation in the plasma chamber and eventually close the LM loop.

4. Model description

We consider a 2D toroidally symmetric domain and perform steady-state calculations. We adopt a multi-fluid description of the plasma and of the neutral species, coupled with a thermal model for the LMD target, providing the wall temperature distribution and the LM evaporation/sputtering rates.

4.1. *SOL plasma model: SOLPS-ITER simulation setup*

We describe the SOL plasma with the SOLPS-ITER code [38]. The full set of charge states is considered for each element included in the simulation, instead of relying on the faster but less accurate bundled charge state model [39], which was used e.g. in [20]. This choice allows for a more detailed description of the atomic loss processes associated to the various plasma species, which play a major role in the power balance in the case of an LMD. In brief, our SOLPS-ITER simulations include the following:

- D^0, D^+ (fuel neutrals and main plasma ions, respectively).
- Li^0, Li^+, Li^{2+}, Li^{3+} (Li vapor and all Li ionized states) in case Li is considered; Sn^0, Sn^+, Sn^{2+}, ..., Sn^{50+} in case Sn is considered.
- Ar^0, Ar^+, Ar^{2+}, ..., Ar^{18+} (for the second set of simulations including Ar seeding).

In the remainder of the paper, for simplicity, we will label the simulations without Ar seeding as "D+Li" or "D+Sn", depending on the LM considered. Simulations with Ar seeding will be labelled as "D+Li+Ar" or "D+Sn+Ar".

Charged species are treated with a multi-fluid approach. We employed a fluid model also for the vapor and fuel neutrals, instead of the kinetic description provided by the EIRENE Monte Carlo neutral transport code available in SOLPS-ITER. This choice allowed performing relatively inexpensive parametric scans at the cost of some approximations. In particular: (i) neutrals in regions of low collisionality are poorly represented by a fluid model, (ii) molecular effects are neglected, and (iii) the effect of condensation on the walls and the actual pumping from the sub-divertor region cannot be properly accounted for, due to the limited extension of the fluid neutral calculation domain, which coincides with the domain for the plasma, shown in Figure 1, and does not extend up to the wall as the EIRENE domain would [40]. For this reason, to mimic pumping and condensation, suitable boundary conditions were imposed on the outermost surface included in the computational domain, as we shall briefly explain in the following.

Nevertheless, the fluid neutral model can provide an acceptable description of the vapor behavior, at least close to the strike point. In that region, (i) the neutral collisionality is large due to the strong source (due to fuel recycling and target erosion), and (ii) pumping ducts are relatively distant, thus rendering a fluid model an acceptable first approximation.

The modelling assumptions are summarized in the following.

- Plasma:
  - Parallel transport is classical, with flux limiting corrections applied for electron and ion heat conductivity, and ion viscosity. The recently updated treatment of friction and thermal forces available in SOLPS-ITER [41] has been used;
  - Perpendicular transport is anomalous. Radial profiles of effective diffusivities for radial transport ($D_\perp$, χ_e, χ_i) are set as code inputs. In particular, $D_\perp$ = 0.42 m^2/s, $\chi_e = \chi_i$ = 0.18 m^2/s in the SOL to reproduce the expected power decay length of λ_q ~ 3 mm, consistently with [42]. In the core, the transport coefficients are varied to simulate the transport barrier.
- Neutrals: as mentioned above, only atoms are considered, for the sake of simplicity.
- Atomic physics: for Li, rates for atomic processes are taken from the ADAS database [43]; for Sn, ADAS baseline (year 89) data were used [44], which however were not yet included in the official ADAS database at the time of writing the present manuscript.
- Drifts and electric currents are neglected, for the sake of simplicity. Recent SOLPS-ITER simulations of the ITER SOL plasma with Ne seeding [45] have shown that the effect of drifts and currents is to increase the extent of the inboard/outboard asymmetry, due to the redistribution of impurities towards the inboard divertor [46]. These effects will be investigated in future extensions of the present work.

The simulation domain, sketched in Figure 1, as well as the quadrilateral grid employed for the calculations, are the same as used in [20]. The domain extends from ~10 cm inside the core plasma (to approximately include the pedestal region) up to ~6 cm deep into the SOL – measured at the outboard midplane, OMP – to include several power decay lengths. In the following, for the sake of simplicity, the outermost magnetic surface included in the domain will be referred to as *wall boundary*.

The boundary conditions for the power balance of the simulation are the following:

- We manually adjust the power P_{in} at the innermost flux surface to ensure P_{SOL} ~ 150 MW crossing the separatrix, which is considered sufficient to allow for H-mode operation [47]. P_{in} is equally split between ions and electrons. The difference between P_{in} and P_{SOL} is associated to radiation losses in the pedestal. Since these losses are more significant for Sn than for Li, using the same value of P_{SOL} for all the simulations allows for a fair comparison between the two LMs, as well as among the different Ar seeding levels considered. It should be noticed that this approach neglects the presence of additional seeded impurities such as, e.g., Xe, used as core radiators. Indeed, more detailed considerations concerning the choice of the core radiator and/or the compatibility of the computed radiation levels in the pedestal with the EU DEMO operational scenario are beyond the scope of this work and left to future studies.
- Targets: the heat deposited on the targets is evaluated assuming a sheath heat transfer coefficient of 2.5 for ions and of 0.90 for electrons, consistently with [20].
- Walls: a radial decay length is imposed on the SOL plasma temperature. The same boundary condition is imposed at the private plasma boundary.

As for the particle balance:

- Core boundary: an incoming D^+ particle flow rate of $5 \cdot 10^{20}$ s^{-1} is set, consistently with [20].
- Targets: fuel ions impinging on the target are assumed to be 100% recycled, whereas other ions (ionized Li/Sn and Ar) are assumed to be 100% deposited. As mentioned above, the target source of vapor and fuel neutrals is computed by an external module, to be described in section 4.2.W
- Walls: a leakage B.C. is imposed both at the wall boundary and at the private plasma boundary. This implies that the outgoing flux is proportional to the local particle density. This condition is selected to simulate the redeposition on the FW.

4.2. External module for determining the surface temperature and target erosion rate

The target thermal model uses the poloidal heat flux profile computed by SOLPS-ITER (which already accounts for the interactions of the plasma with the vapor and the fuel neutrals) and the active cooling parameters (coolant inlet temperature and pressure, and heat transfer coefficient) as inputs. It then computes the poloidal profile of the divertor target surface temperature, and the corresponding sputtering and evaporation profiles. Due to the slow motion of the LM in the CPS (few mm/s) and based on the assumption that no droplet ejection nor splashing occur, the CPS+LM system is treated as a stationary solid medium having an equivalent thermal conductivity, computed according to relative volume occupied by LM and CPS, as suggested in [48].

For the flat plate concept considered for Li shown in Figure 2 (a), a simple 1D heat conduction model (in the direction normal to the target) is adopted to determine the target temperature at each poloidal target location, similar to [27]. For Sn, to account for the actual target geometry, the more accurate, quasi-3D model presented in [49] has been adopted, after having been extended to include an LM-filled Capillary-Porous Structure (CPS) on top of the CuCrZr heat sink.

Once the target temperature profile is known, the *gross* erosion particle flux ($s^{-1}m^{-2}$) is evaluated following [32] as:

$$\Gamma_{Li/Sn,gross} = \sum_j \left\{ \Gamma_j \left[(1 - f_{ion}) \cdot Y_{p,j\rightarrow Li/Sn}(E_j) + Y_t \right] \right\} + \eta \cdot \frac{p_{v,Li/Sn}(T) - p_a}{\sqrt{2\pi m_{Li/Sn} k T_{Li/Sn}}} \tag{1}$$

where j runs over all the ion species. Γ_j is the ion flux at the target and E_j is the energy of the impinging ion j. $Y_{p,j\rightarrow Li/Sn}$ is the physical sputtering yield for the impact of ion j on a liquid Li/Sn surface, evaluated according to [50]. $Y_{p,j\rightarrow Li/Sn}$ is multiplied by a factor $(1 - f_{ion})$ to account for sputtered ions, as mentioned in section 3. For Li, as mentioned above, f_{ion}= 2/3, whereas for Sn ion emission can be neglected. Y_t is the thermal sputtering yield, which in the case of Li is evaluated according to the Adatom thermal sputtering model:

$$Y_t = \frac{Y_{ad}}{1 + A \exp\left(\frac{E_{eff}}{kT}\right)} \tag{2}$$

where the constants Y_{ad} = 2.9, $A = 9.6 \cdot 10^{-6}$ and E_{eff} = 0.7 eV are fitting parameters [34]. It should be noticed that these fitting parameters have been obtained for D^+ impinging on liquid Li. Due to the lack of relevant data in the available literature, here we employ the same parameters for thermal sputtering associated to the impingement of other ions (Li or Ar), as suggested in [51]. For Sn, thermal sputtering is instead neglected (Y_t = 0), due to lack of data. In the evaporation term, the sticking coefficient η is set to 0.75, as suggested in [52], but it should be noticed that this quantity is subject to uncertainties. $p_{v,Li/Sn}(T)$ is the vapor pressure of the LM evaluated at the target temperature, and p_a is the pressure in front of the target. We set $p_a \sim 0$, consistently with [27], even though it is worth mentioning that other studies suggest to assume $p_a \sim p_{plasma}$ [11,53]. The profile of the *net* erosion particle flux along the target is computed by applying a poloidally variable prompt redeposition coefficient [54], accounting for the local plasma conditions in front of the target:

$$\Gamma_{Li/Sn,net} = \Gamma_{Li/Sn,gross} \cdot \left(1 - f_{redep}\right) \tag{3}$$

As mentioned above, discussing the implications of $\Gamma_{Li/Sn,net}$ in terms of recollection of the metal from the FW is beyond the scope of the present work. However, it is stressed that the capability of computing this quantity self-consistently, which is demonstrated in this paper, is essential to enable future studies on this matter.

5. Results and discussion

To assess the effect of the presence of an LMD in different reactor operating conditions, we performed parametric studies varying the upstream electron density at the OMP separatrix, $n_{e,sep}$. We selected the range $3.5 \cdot 10^{19}$ $m^{-3} < n_{e,sep} < 4.5 \cdot 10^{19}$ m^{-3}, corresponding to ~ 40% - 52% of the Greenwald density [3]. This range, albeit relatively small, allows to appreciate the trends in the quantities relevant for the present work.

After presenting the results of D+Li and D+Sn simulations, we will consider the effect of Ar seeding as an attempt to reduce the target erosion rate and heat flux.

5.1. Results without Ar seeding

We begin discussing the particle balance, starting from the source term for the vapor, i.e. the target erosion rate. Figure 3 shows that, as expected, the total (net) erosion rate for Li (Γ_{Li}) is ~2 orders of magnitude larger than the total (net) erosion rate for Sn (Γ_{Sn}). For Li, evaporation represents the dominant erosion mechanism, and the relative contributions of the three erosion mechanisms considered is weakly dependent on $n_{e,sep}$. For Sn, consistently with the results presented in [51], evaporation is again found to be the dominant erosion mechanism, especially at large values of $n_{e,sep}$.

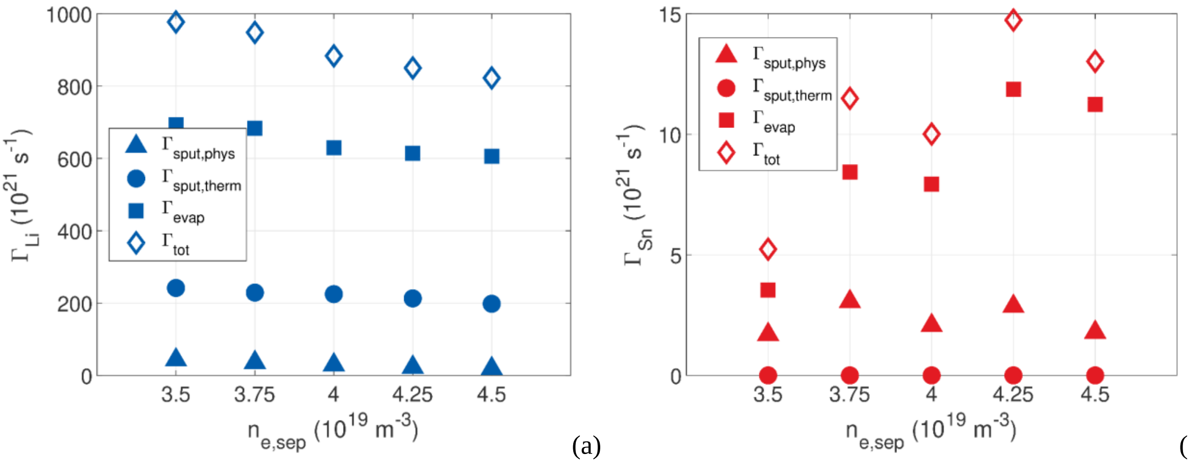

(a) (b)

Figure 3. Total target erosion rate as a function of $n_{e,sep}$, for Li (a) and for Sn (b). The different contributions to the target erosion are also indicated. Note the different y scale.

For Li, the three contributions to the target erosion (evaporation, thermal sputtering and physical sputtering) all show an inverse dependence on $n_{e,sep}$. As far as the sputtering rate is concerned, this behavior is consistent with simple two-point model considerations [55], since increasing $n_{e,sep}$ leads to a reduced target electron temperature, and therefore lower erosion, according to equation (1). Moreover, as shown in Figure 4 (a), the radiation rate in front of the Outboard Target (OT) associated to Li vapor shielding, $q^{Li}_{rad,OT}$, increases with $n_{e,sep}$, thus further decreasing the target electron temperature. This can be explained in terms of the radiated power density $L_Z^{Li}(T_e,n_e) \cdot n_{Li} \cdot n_e$, where the increase in n_e more than compensates for the lower n_{Li} due to the weaker erosion. The same trend is observed in the power radiated via interactions with fuel neutrals $q^{D}_{rad,OT}$. The stronger radiation in front of the OT also leads to a mitigation of the heat flux to the target and, consequently, to a lower target surface temperature, which explains the trend in thermal sputtering and evaporation. It should be noticed that another effect contributing to reduce the erosion rate is the increase of the prompt redeposition rate with $n_{e,sep}$ (not reported here). For the Inboard Target (IT) the same trend is observed, but we do not report it here, since IT erosion only accounts for a small percentage of the total.

For Sn, having neglected thermal sputtering, only physical sputtering and evaporation contribute to the erosion rate. Figure 3 (b) shows that the physical sputtering rate remains almost constant with $n_{e,sep}$, while the evaporation rate globally increases, although both quantities show a non-monotonic behavior. This can be explained in terms of two competing effects: the radiation in the OT region due to Sn vapor shielding $q^{Sn}_{rad,OT}$ decreases as $n_{e,sep}$ increases, dominating over the increase in $q^{D}_{rad,OT}$, as shown in Figure 4 (b). This tends to determine a larger target electron temperature and heat flux. Conversely, as for Sn, the prompt redeposition rate increases as $n_{e,sep}$ increases.

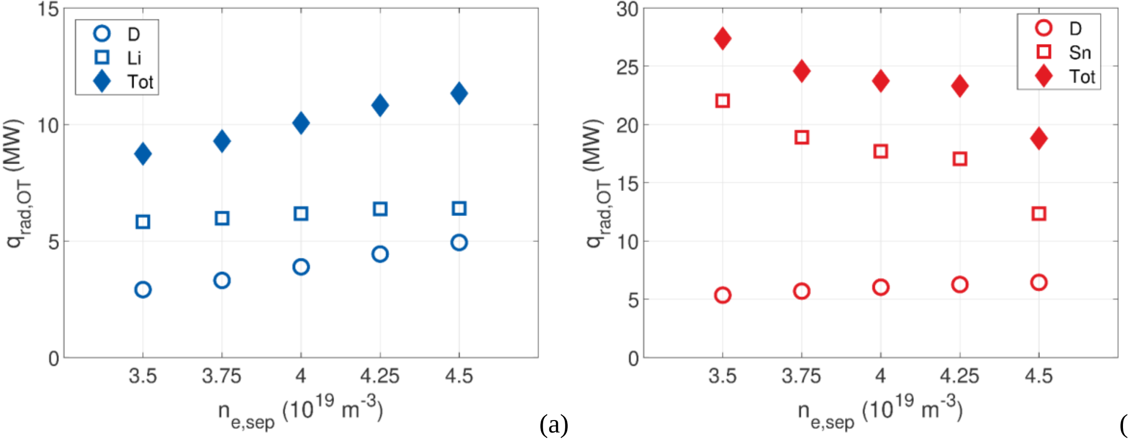

(a) (b)

Figure 4. Radiated power density due to D and Li/Sn integrated over the OT region, for Li (a) and for Sn (b). Note the different y scale.

Figure 5 shows the resulting distribution of impurity concentration ($n_{Li/Sn}/n_e$, summed over the whole set of ionization stages) in the simulated domain, for the cases corresponding to $n_{e,sep}$ = 4.5 · 10^{19} m^{-3}. For both Li and Sn, the largest concentration is found close to the OT strike point (where the strongest Li/Sn source is located) and in the far SOL, where n_e is low. As anticipated above, the strong asymmetry between conditions at IT and at OT is associated to the inboard/outboard heat load asymmetry. Indeed, due to the lower heat flux on the IT, the surface temperature is lower, and so the evaporation rate. The low ion temperature at the IT also causes limited sputtering. As already mentioned, this asymmetry is probably underestimated, having neglected drifts. Figure 6 (a) shows the computed relative abundances of Li^0, Li$^+$, Li^{2+} and Li^{3+} with respect to the total Li density, while Figure 6 (b) shows the computed relative abundances of Sn^0, Sn^{3+}, Sn^{10+} and Sn^{20+} with respect to the total Sn density, again for the cases corresponding to $n_{e,sep}$ = 4.5 · 10^{19} m^{-3}. As expected, Li is fully ionized over a large part of the computational domain, whereas for Sn the SOL is characterized by the presence of Sn$^+$ - Sn^{20+}.

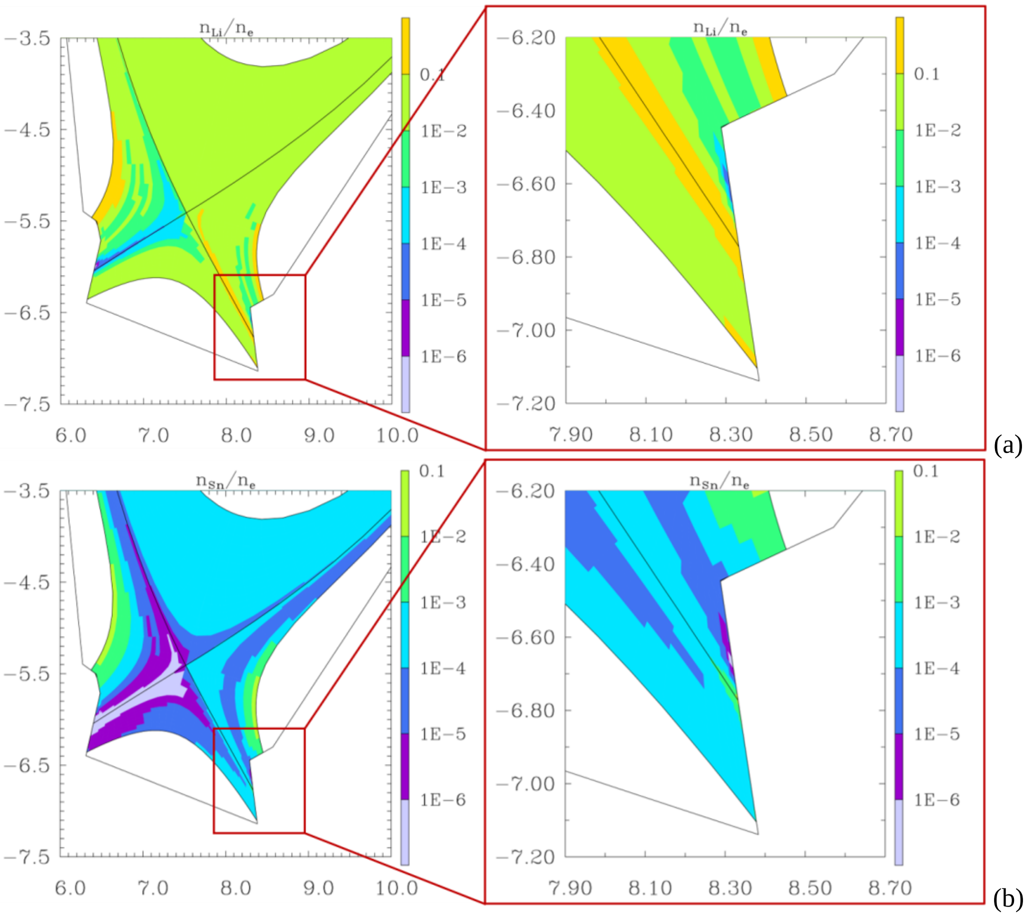

Figure 5. Computed 2D distributions of the relative concentrations n_{Li}/n_e (a) and n_{Sn}/n_e (b) in the edge plasma for the case $n_{e,sep}$ = 4.5 · 10^{19} m^{-3}, with an enlargement showing the conditions in front of the OT.

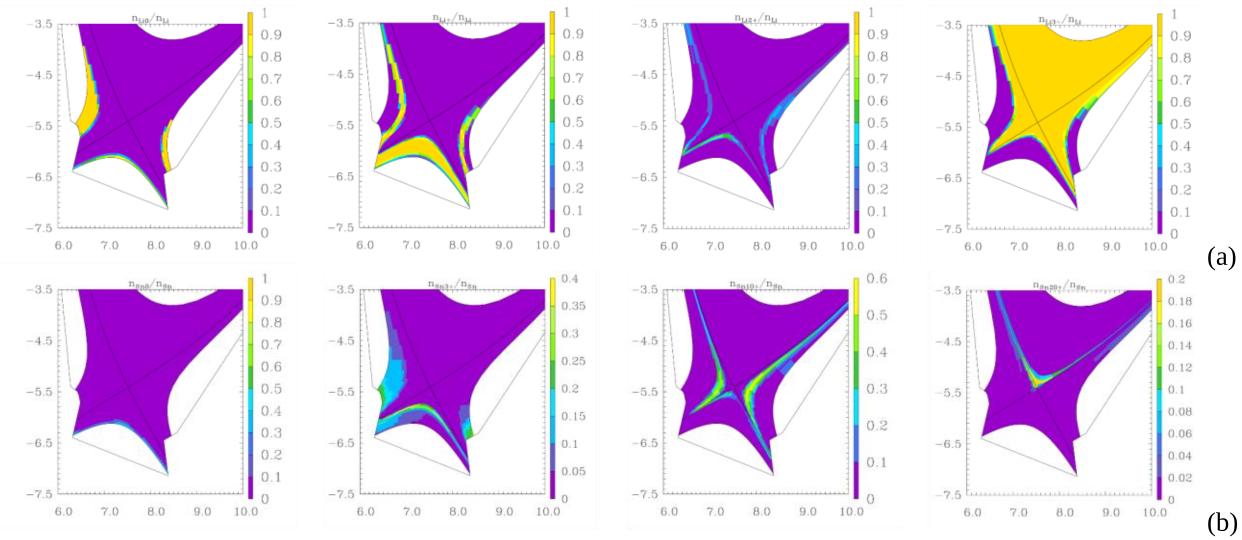

Figure 6. Computed 2D distributions of the relative abundance of Li^0, Li^+, Li^{2+}, $Li^{3+}$with respect of the total Li density (a) and of Sn^0, Sn^{3+}, Sn^{10+}, $Sn^{20+}$with respect of the total Sn density (b) in the edge plasma for the case with $n_{e,sep}$ = 4.5 · 10^{19} m^{-3}. The ionization stage increases moving from left to right. Note that for Sn the y scale has been varied among the four plots for the sake of readability.

Figure 7 (left) compares Li and Sn in terms of average impurity concentration in the pedestal, $\langle n_{Li/Sn}/n_e\rangle_{pedestal}$. Also indicated in the plot are "plasma cleanness limits" which have been calculated in [56] based on integrated target-SOL-core simulations performed with the COREDIV code: $\langle n_{Li}/n_e\rangle_{\ pedestal}$ < 3% for Li (corresponding to a ~20% reduction of the fusion power with respect to the case of pure D-T plasma) and $\langle n_{Sn}/n_e\rangle_{\ pedestal}$ <0.05% for Sn (corresponding to a back-transition from H to L mode due to the reduction of P_{sep} following from excessive core radiation). Our results indicate that, for Li, plasma dilution is an issue, for the entire range of $n_{e,sep}$ considered in the present study. For Sn, instead, the concentration is ~ 2 orders of magnitude lower with respect to the case of Li, and at sufficiently large values of $n_{e,sep}$ it is lower than the above-mentioned "plasma cleanness limit", thus suggesting the existence of an operational window for which an Sn divertor is compatible with the EU DEMO core plasma performance requirements. The corresponding value of the effective charge Z_{eff} averaged over the pedestal region included in the simulation domain, $\langle Z_{eff}\rangle_{pedestal}$, is reported in Figure 7 (right). It is noticed that a more careful assessment of the core plasma conditions, achieved by e.g. coupling SOLPS-ITER to a core transport code, should be performed to allow for a fully self-consistent calculation of the SOL and core conditions in the presence of an LMD, thus enabling more quantitative conclusions on the core plasma compatibility of this concept to be drawn.

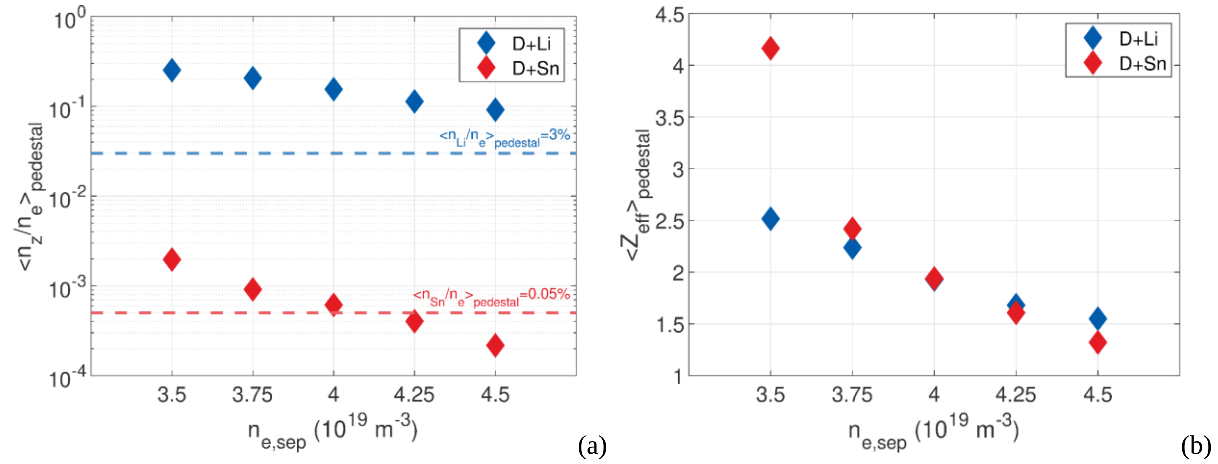

Figure 7. Impurity concentration (Li or Sn) averaged over the pedestal region (a) and average Z_{eff} in the pedestal region: comparison Li vs. Sn (b).

We now discuss the power balance. Figure 4, which was shown before to support the discussion concerning the trends in erosion rate for Li and Sn, already indicated a stronger OT radiation for Sn with respect to Li. In Figure 8, the distributions of the radiated power density for Li and Sn are compared, for the case corresponding to $n_{e,sep}$ = 4.5 · 10^{19} m^{-3}. In this respect, as it could be expected from the charge stage distributions shown in Figure 6, Li performs better than Sn, since it causes beneficial plasma cooling in front of the target, while only negligibly radiating in the core plasma, where it exists almost only in the fully stripped charge state. However, this was already shown to be insufficient to prevent an excessive core plasma dilution associated to the presence of Li. For Sn, a non-negligible pedestal radiation is found, which however was shown above to be marginally compatible with core plasma performance. The other main qualitative difference with respect to Li is the significant radiation along the SOL (not just in front of the OT). This fact implies a mitigation of the plasma power entering the *vapor shielding* region in front of the target, thus reducing the evaporation rate necessary to sustain the vapor shielding regime.

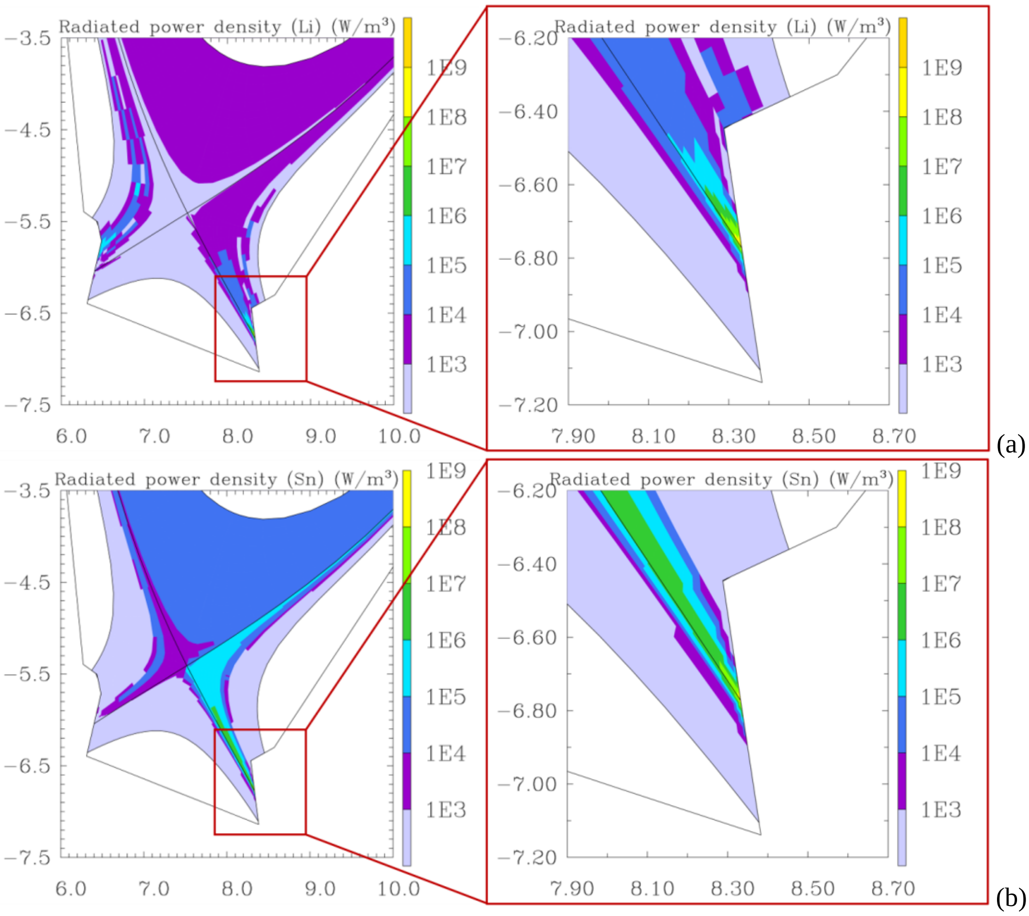

Figure 8. Computed 2D distributions of the radiated power density for Li (a) and Sn (b), for the case $n_{e,sep}$ = 4.5 · 10^{19} m^{-3}, with an enlargement showing the conditions in front of the OT.

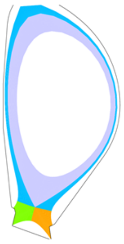

Total radiated power (MW)		OT	IT	SOL	Pedestal	TOT
	D+Li	11	8	3	3	25
	D+Sn	19	1	11	19	50

Table 1 summarizes the total radiated power (due to the metal vapor, ions, fuel neutrals and main plasma ions) integrated over different regions of the computational domain, for the case $n_{e,sep}$ = 4.5 · 10^{19} m^{-3}. As it was already evident from the 2D plots of Figure 8, radiation in the pedestal and along the SOL is significant for Sn, whereas it is negligible for Li. It is noticed that, due to this fact, for the case with Sn at $n_{e,sep}$ = 4.5 · 10^{19} m^{-3} we had to increase P_{in} up to ~170 MW, to keep P_{SOL} ~ 150 MW (the latter choice was motivated in section 4.1). The required P_{in} was larger at lower values of $n_{e,sep}$, due to a more significant pedestal radiation. The situation is more balanced in the OT region, where still Sn radiates more. Finally, for Li a weaker inboard-outboard asymmetry in plasma cooling is computed, due to non-negligible target erosion observed also at the inboard target.

Table 1. Schematic of the simulation domain with the regions highlighted and summary table of the total radiated power density integrated over different regions of the simulation domain for the cases D+Li and D+Sn, for $n_{e,sep}$ = 4.5 · 10^{19} m^{-3}.

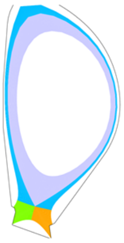

Total radiated power (MW)		OT	IT	SOL	Pedestal	TOT
	D+Li	11	8	3	3	25
	D+Sn	19	1	11	19	50

We conclude assessing the effect of plasma-vapor interactions on the target heat flux. To support this discussion, in Figure 9 we plot the computed heat flux profiles on the OT for the case $n_{e,sep} = 4.5 \cdot 10^{19}$ m^{-3}, for both Li and Sn. On the same plot, we report as a reference the heat flux for a pure D plasma, computed using a consistent simulation setup. The beneficial reduction of the target heat flux (~50% for Li and ~30% for Sn) associated to the vapor shielding effect, for the cases where an LM target is adopted, is evident. Nevertheless, the peak heat load for Li (~31 MW/m^2) is larger than the power handling limit of the specific target design here considered, i.e. ~20 MW/m^2. Similarly, the peak heat load for Sn (~44 MW/m^2) is slightly larger than the power handling limit of the ENEA target design, i.e. ~40 MW/m^2. The corresponding peak temperatures are ~900°C for Li and ~1700°C for Sn. These temperatures are responsible for the significant target evaporation, which represents the dominant contribution to the erosion rate, as discussed above.

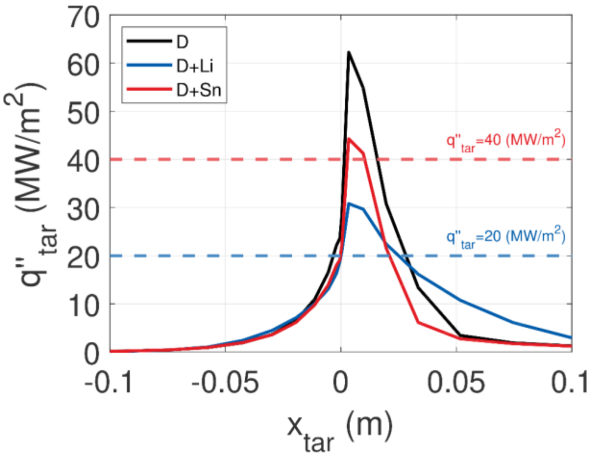

Figure 9. Target profiles of plasma advection/conduction heat flux for the cases D+Li and D+Sn compared with a reference case with pure D, for $n_{e,sep} = 4.5 \cdot 10^{19}$ m^{-3}.

For both Li and Sn, the heat flux computed by SOLPS-ITER far from the strike point appears to be negligible. However, this calculation does not take into account the possibly relevant radiative heat flux. For this reason, we evaluated the radiative contribution $q''_{rad,tar}$ to the heat load on the outboard divertor. This could be useful e.g. to determine whether the temperature far from the strike point is lower than the Li retention limit, or to estimate whether radiation can be sufficient to keep the LM molten throughout the whole target. The radiation load was estimated with the Monte Carlo ray-tracing code CHERAB [57–60] for the case $n_{e,sep} = 4.5 \cdot 10^{19}$ m^{-3}, without Ar seeding, see Figure 10. The estimated peak value of $q''_{rad,tar}$ is $1.33\,\mathrm{MW/m^2}$ in the case of Li and $1.97\,\mathrm{MW/m^2}$ with Sn, i.e. ~4% and ~6% of the advection/conduction peak heat flux shown in Figure 9, respectively. Away from the strike point, moving upwards along the OT, the relative contribution of the radiative heat load increases to ~30% for Li and ~80% for Sn (at x_{tar} = 0.2 m). This indicates that, notwithstanding the additional heat load contribution associated to radiation, the LM will freeze far from the strike points (at least with the target cooling schemes here considered).

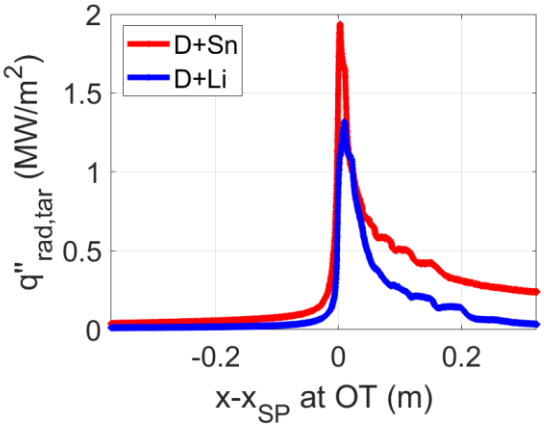

Figure 10. Outboard target profiles of radiation heat load computed for Li and Sn, for $n_{e,sep}$ *= 4.5 · 10*^{19} *m*$^{-3}$*.*

Summarizing the results of this section:

- For Li, an excessive plasma dilution is computed, for the entire range of $n_{e,sep}$ considered in this study. Moreover, notwithstanding the self-regulation of the target heat flux, the power handling limit of the technological solution here considered is overcome.
- For Sn, our calculations suggest that plasma contamination could be tolerable, at sufficiently large values of $n_{e,sep}$. Nevertheless, the peak heat flux on the target is found to be slightly larger than the heat handling limit of the proposed technological solution for the target itself, notwithstanding the self-regulation provided by vapor shielding.

These results suggest that the operational window for Li or Sn target employed for the EU DEMO without any additional impurity seeding might be too narrow, if it exists, with Sn being more promising than Li, at least for the ITER-like target configuration considered in this work. This motivates further calculations to assess the effect of purposely seeding an additional impurity (e.g. Ar). Thanks to the additional plasma cooling provided by Ar, the target heat flux is expected to be reduced, so lowering the metal erosion rate, eventually also limiting the core contamination.

5.2. Results with Ar seeding

For this second set of simulations, we injected Ar from the wall boundary of the calculation domain with a uniform distribution, while a detailed study on the optimization of the injection location is beyond the scope of the present work. Three Ar seeding rates, $\Gamma_{Ar} = 5 \cdot 10^{20}$ s^{-1}, $\Gamma_{Ar} = 7 \cdot 10^{20}$ s^{-1}, $\Gamma_{Ar} = 1 \cdot 10^{21}$ s^{-1}, were considered, consistent with [20].

5.2.1. Particle balance

Figure 11 confirms the effectiveness of Ar injection in reducing the target erosion. In particular, at high densities, even the lowest Ar seeding rate here considered ($\Gamma_{Ar} = 5 \cdot 10^{20}$ s^{-1}) is capable of reducing the erosion rate by approximately one order of magnitude, for both Li and Sn. To better understand this behavior, Figure 12 shows the various contributions to the erosion rate for all the values of $n_{e,sep}$ and $\Gamma_{Ar,SOL}$ here considered, for both Li and Sn. The observed reduction in both evaporation and sputtering can be correlated to the power radiated in the SOL due to interactions with the seeded Ar, shown in Figure 13. Indeed, the power radiated along the SOL (i) determines a reduction in the electron temperature, which implies a lower sputtering rate, and (ii) reduces the power entering the "vapor shielding region" in front of the OT, thus lowering the evaporation rate. For Li, which does not significantly radiate far from the target – where it exists mostly in fully ionized state – the presence of Ar determines a significant increase in the SOL radiation rate with respect to the D+Li case. For Sn, instead, Ar radiation in the SOL has to compensate for the previously significant Sn radiation in the same region. This compensation is always effective, except for the case with $n_{e,sep} = 3.5 \cdot 10^{19}$ m^{-3} and $\Gamma_{Ar} = 5 \cdot 10^{20}$ s^{-1}, where the increase in Ar SOL radiation is not sufficient to make up for the lower Sn SOL radiation with respect to the corresponding case without Ar seeding. This explains the non-monotonic trend in Γ_{Sn} with increasing Γ_{Ar} for $n_{e,sep} = 3.5 \cdot 10^{19}$ m^{-3}. For a given Ar seeding rate, increasing $n_{e,sep}$ is found to always lead to a reduction in the erosion rate. This is due to the fact that the Ar radiation $P_{rad} = L_Z^{Ar}(T_e, n_e) \cdot n_{Ar} \cdot n_e$, which increases with increasing $n_{e,sep}$ due to the global increase of n_e, dominates the SOL power balance for both Li and Sn, as shown in Figure 13.

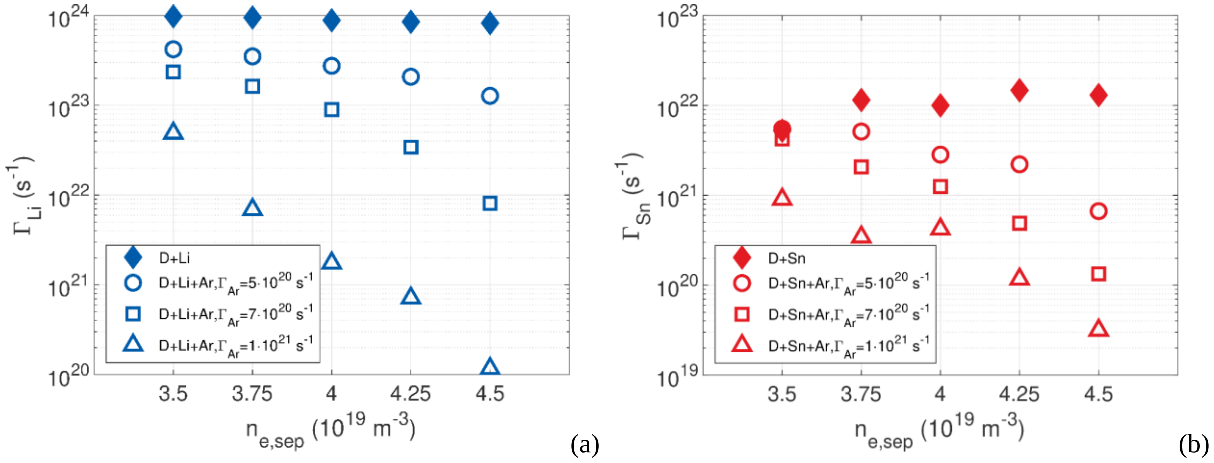

(a) (b)

Figure 11. Total target erosion rate as a function of $n_{e,sep}$ *for the different Ar seeding rates considered in this work, for Li (a) and for Sn (b). Note the different y scale.*

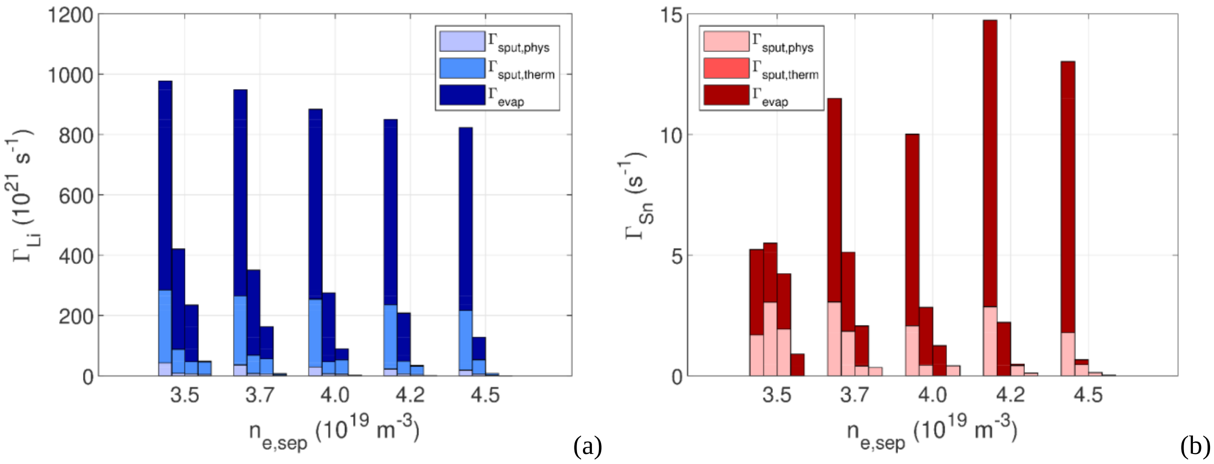

(a) (b)

Figure 12. Contributions to the target erosion rate for Li (a) and Sn (b). For each value of $n_{e,sep}$, *the four bars correspond to increasing (left to right) Ar seeding levels, from* Γ_{Ar} *= 0 to* Γ_{Ar} *= 1·10^{21} s^{-1}. Note the different y scale.*

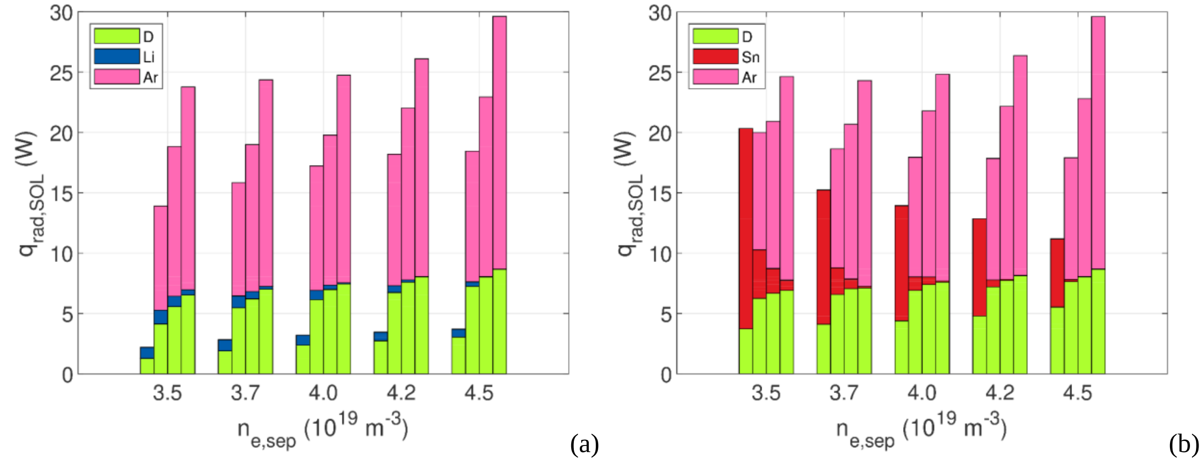

(a) (b)

Figure 13. Contributions to the radiated power density, integrated over the SOL region, for Li (a) and Sn (b). For each value of $n_{e,sep}$, *the four bars correspond to increasing (left to right) Ar seeding levels, from* Γ_{Ar} *= 0 to* Γ_{Ar} *= 1·10^{21} s^{-1}.*

Figure 14 shows the resulting distribution of impurity concentration ($n_{Li/Sn}/n_e$) in the simulated domain, for the cases corresponding to $n_{e,sep}$ = 4.5 · 10^{19} m^{-3}, for the various Ar seeding rates considered in this work. The reduced target erosion rate determined by Ar seeding clearly results in a lower Li/Sn concentration over the whole computational domain. The concentration remains relatively large in the far SOL and in the private flux region, where the electron density is low.

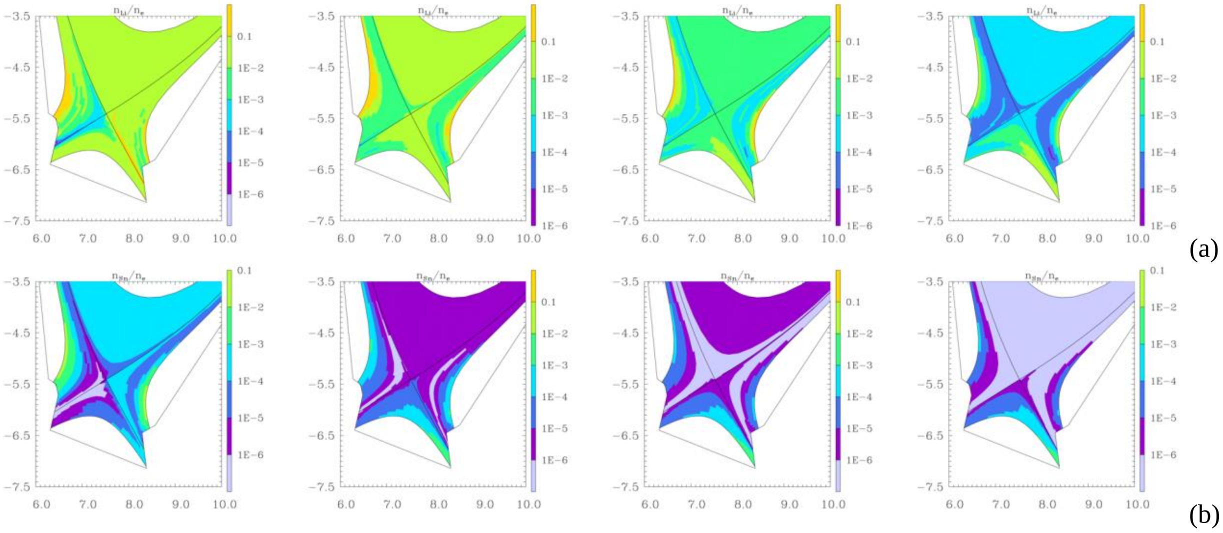

Figure 14. Computed 2D distributions of the relative concentrations n_{Li}/n_e (a) and n_{Sn}/n_e (b) in the edge plasma for the cases with $n_{e,sep}$ = $4.5 \cdot 10^{19}$ m^{-3}, for increasing Ar seeding rates (from Γ_{Ar} = 0 to Γ_{Ar} = $1 \cdot 10^{21}$ s^{-1}, moving from left to right).

To support a more quantitative discussion, in Figure 15 we plot the Li/Sn density averaged over the pedestal region, for the entire set of $n_{e,sep}$ and Γ_{Ar} considered in this work, and compare it to the above-mentioned "plasma cleanness limits". Consistently with the results shown in Figure 11, Figure 12 and Figure 14, for a given $n_{e,sep}$, a larger Γ_{Ar} determines a lower concentration in the pedestal. As a consequence, the allowed operational window for the LMD concepts considered in this paper, in terms of core plasma performance, appears to be significantly widened.

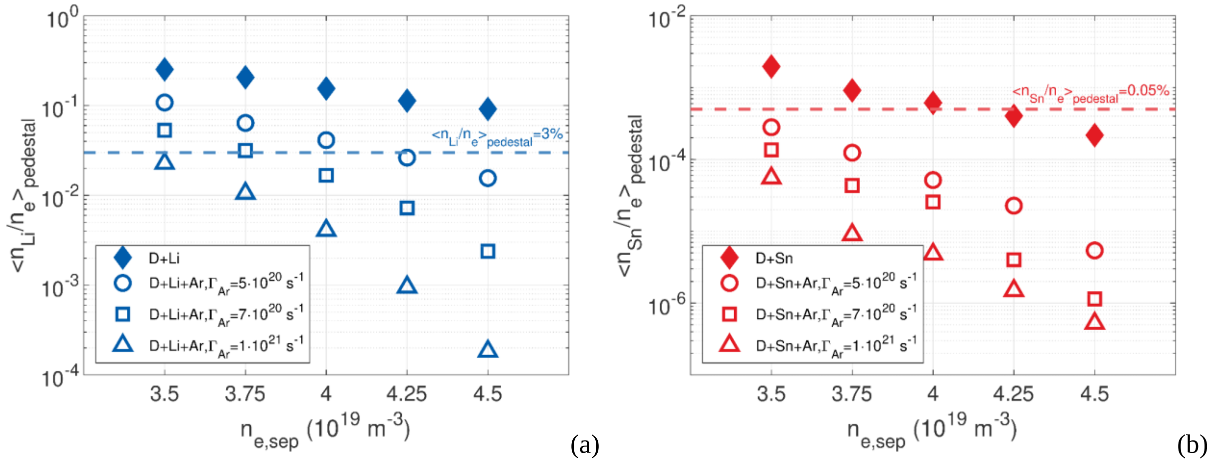

Figure 15. Impurity concentration (Li or Sn) averaged over the pedestal region, for various Ar seeding intensities: Li (a) and Sn (b). Note the different y scale.

The beneficial effect of Ar seeding in terms of the improvement of the core plasma compatibility of an LMD is reflected by the significant reduction of the effective charge Z_{eff} averaged over the pedestal, $\langle Z_{eff} \rangle_{pedestal}$, shown in Figure 16 (a) for the cases $\Gamma_{Ar} = 0$ and $\Gamma_{Ar} = 1.0 \cdot 10^{21}$ $(\#/s)$. This result indicates that, while Ar seeding is effective in mitigating the plasma power load to the divertor targets (mostly thanks to SOL radiation, as discussed above), it does not represent a threat for the core plasma purity, at least for the values of Γ_{Ar} considered in this work. Another interesting feature of the result shown in Figure 16 is that, for Γ_{Ar} = $1 \cdot 10^{21}$ s^{-1}, the difference between the cases D+Li+Ar and D+Sn+Ar in terms of $\langle Z_{eff} \rangle_{pedestal}$ becomes negligible. This is a consequence of the fact that Ar represents the dominant plasma impurity for these cases, whereas the density of Li/Sn is negligible. To complete the discussion, Figure 16 (b) shows the radiated power density, integrated over the pedestal region, for the cases $\Gamma_{Ar} = 0$ and Γ_{Ar} = $1 \cdot 10^{21}$ s^{-1}. For Li, the reduction of the core plasma dilution associated to Ar occurs at the expense of a slight increase of core radiation due to the presence of Ar (whereas core radiation due to Li was negligible). For Sn, instead, the reduction of the core plasma radiation associated to Sn more than compensates for the moderate increase in radiation associated to Ar. Again, for the case Γ_{Ar} = $1 \cdot 10^{21}$ s^{-1} a very similar behavior is observed for the cases D+Li+Ar and D+Sn+Ar.

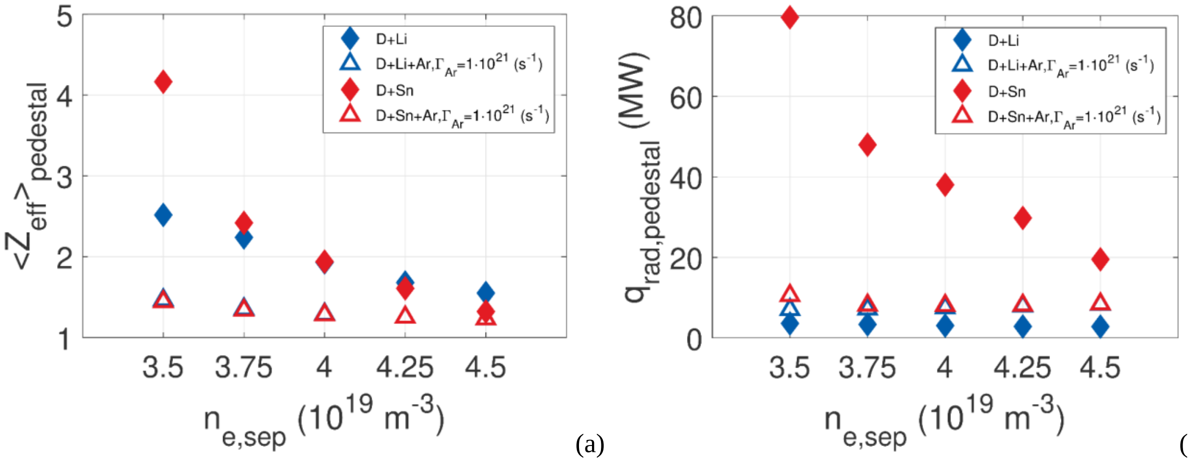

Figure 16. Average Zeff in the pedestal region for different Ar seeding rates: comparison Li vs. Sn (a), and radiated power density integrated over the pedestal region for various Ar seeding rates: comparison Li vs. Sn (b). Only the cases with Γ_{Ar} = 0 and Γ_{Ar} = 1·10^{21} s^{-1} are shown, for clarity.

To summarize the discussion on the particle balance for the cases with Ar seeding, it can be stated that the operational window for an LMD in terms of core plasma compatibility appears significantly widened, for both Li and Ar. Moreover, even though a detailed discussion on the LM recollection from the FW is beyond the scope of the present work, the reduction of the net erosion rate (by more than 2 orders of magnitude, for the largest $n_{e,sep}$ considered) might significantly affect the design of the recollection system, or even make it unnecessary.

5.2.2. Power balance

The results reported in Figure 13, which we have already commented while discussing the mitigation of the target erosion rate associated with Ar seeding, indicate that Ar represents the dominant contribution to SOL radiation, for all the values of $n_{e,sep}$ and Γ_{Ar} considered in this study. Moreover, Figure 16 showed how the radiation in the core is reduced for the case D+Sn+Ar with respect to the case D+Sn thanks to the lower Sn erosion rate. To better visualize these effects, we plot in Figure 17 the distribution of the radiated power density for the cases D+Li and D+Li+Ar (a), and D+Sn and D+Sn+Ar (b) corresponding to $n_{e,sep}$ = 4.5 · 10^{19} m^{-3}, for all the Ar seeding rates considered. The similarity between the cases D+Li+Ar and D+Sn+Ar is associated to the fact that, as discussed above, Ar radiation becomes the dominant contribution to the power balance in both the SOL and the pedestal. Figure 18 shows that, in the OT region, for the lowest values of Γ_{Ar} considered, the vapor shielding (i.e. radiation associated to the interactions with the eroded Li or Sn) still plays a non-negligible role. However, as Γ_{Ar} is further increased, this effect reduced, as the function of mitigating the heat load is performed by Ar. We can therefore conclude that *purposely seeding Ar allows to move from a vapor shielding regime, where the heat load mitigation is performed by the eroded metal close to the OT, to a regime in which the mitigation of the plasma power leaving the separatrix occurs in the SOL due to Ar radiation*. It should however be noticed that, even though vapor shielding is not exploited as a heat load mitigation mechanism during normal operation, it could still provide target self-protection in the case of off-normal events such as disruptions or unmitigated ELMs, as suggested in [19].

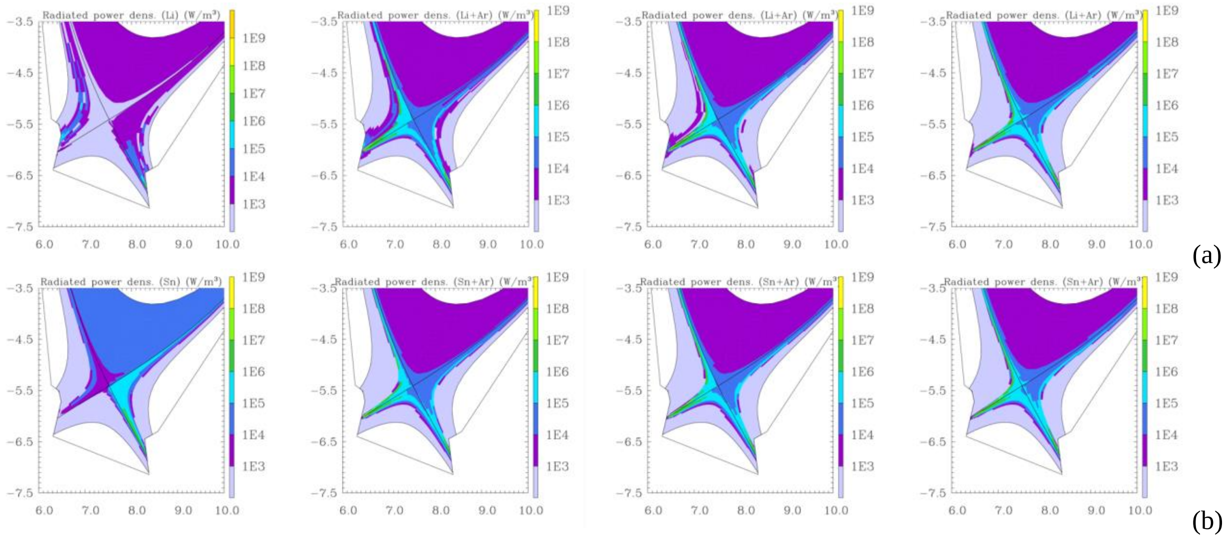

Figure 17. Computed 2D distributions of the radiated power density associated to Li+Ar (a) and Sn+Ar (b) in the edge plasma, for the cases with $n_{e,sep} = 4.5 \cdot 10^{19}$ *m*$^{-3}$*, for increasing Ar seeding rates (from* $\Gamma_{Ar} = 0$ *to* $\Gamma_{Ar} = 1 \cdot 10^{21}$ *s*$^{-1}$*, moving from left to right).*

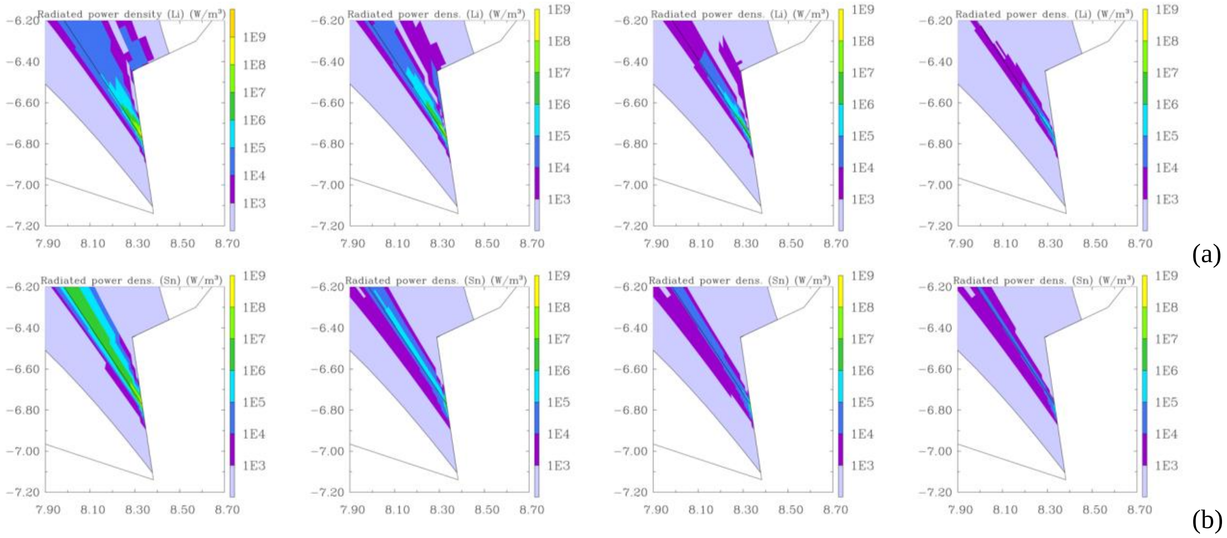

Figure 18. Computed 2D distributions of the radiated power density (W/m^3*) associated to Li (a) and Sn (b) close to the OT for the cases with* $n_{e,sep} = 4.5 \cdot 10^{19}$ *m*$^{-3}$*, for increasing Ar seeding rates (from* $\Gamma_{Ar} = 0$ *to* $\Gamma_{Ar} = 1 \cdot 10^{21}$ *s*$^{-1}$*, moving from left to right).*

To have a glance of the parametric dependences of the effects just described, we analyze the power radiated in the various regions of the calculation domain in more detail, distinguishing among the contributions of the various species. Figure 19 (a) shows that, for the case D+Li+Ar, Ar determines the anticipated increase of the power radiated in the pedestal. This increase is significant in relative terms, but it is not believed to represent a threat for core plasma performance, since the Ar concentration in the pedestal always remains below the tolerability limit computed in [61], i.e. ~0.5%. Figure 19 (b) instead shows that, for the case D+Sn+Ar, the dominant effect in the pedestal is the reduction of Sn radiation due to the lower Sn content. Figure 20 (a) indicates that, for Li, Ar radiation in the OT more or less compensates for the reduced vapor shielding effect, especially at large densities. Figure 20 (b), instead, indicates that for Sn the dominant effect in front of the OT is the reduction in Sn radiation. This is made possible by Ar radiation in the SOL, as already pointed out by results in Figure 13).

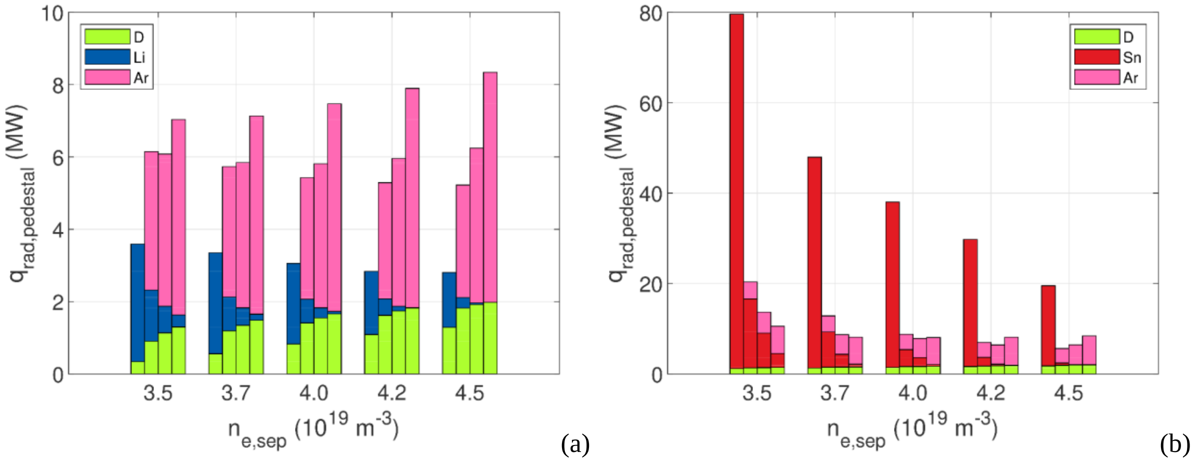

Figure 19. Contributions to the radiated power density, integrated over the pedestal region, for Li (a) and Sn (b). For each value of $n_{e,sep}$*, the four bars correspond to increasing Ar seeding levels, from* $\Gamma_{Ar} = 0$ *to* $\Gamma_{Ar} = 1 \cdot 10^{21}$ *s*$^{-1}$*. Note the different scales.*

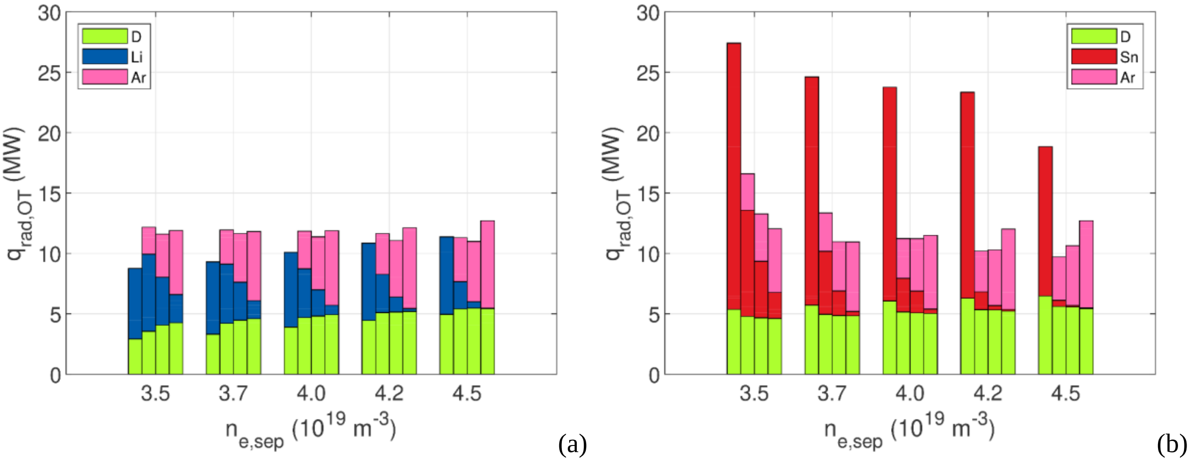

Figure 20. Contributions to the radiated power density, integrated over the OT region, for Li (a) and Sn (b). For each value of $n_{e,sep}$, the four bars correspond to increasing Ar seeding levels, from Γ_{Ar} = 0 to Γ_{Ar} = $1 \cdot 10^{21}$ s^{-1}.

Having shown the effectiveness of Ar seeding in mitigating the erosion rate and the plasma contamination, we conclude discussing the reduction of the heat flux on the OT – which is the most loaded between the two targets. To this aim, in Figure 21 we show the target heat flux profiles for the case $n_{e,sep} = 4.5 \cdot 10^{19}$ m^{-3}, for the various Ar seeding rates considered. For both Li and Sn, the peak heat flux is reduced by a factor up to ~2, which is sufficient to ensure compliance with the power handling limit of the LMD designs considered in this work. These results suggest that LMDs based on the CPS concept using either Li or Sn, if used in combination with Ar seeding, could be compliant with the EU DEMO plasma scenario in terms of both plasma dilution/contamination and target heat handling limit. We also note that Sn appears to have a wider operational window with respect to Li, in terms of minimum $n_{e,sep}$ and Γ_{Ar} required to satisfy the above-mentioned constraints.

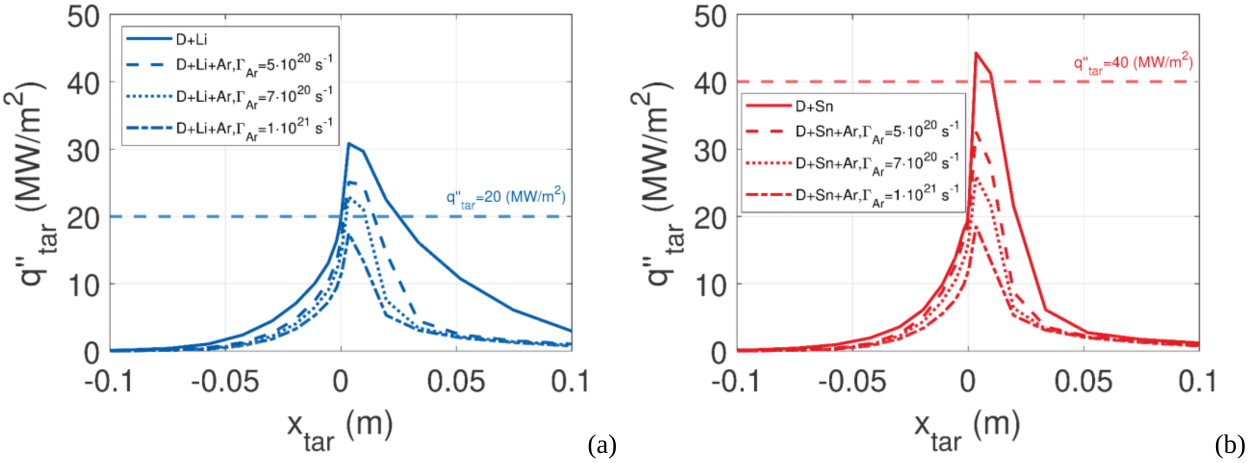

Figure 21. Outboard target profiles of plasma advection/conduction heat flux for D+Li+Ar (a) and D+Sn+Ar (b), for the various Ar seeding rates considered, for $n_{e,sep} = 4.5 \cdot 10^{19}$ m^{-3}.

6. Conclusions and perspective

In this work, we studied for the first time the EU DEMO SOL plasma behaviour, in the presence of a CPS-based LMD using either Li or Sn, by means of the SOLPS-ITER code. Target evaporation and sputtering were calculated self-consistently by coupling SOLPS-ITER with a thermal model for the solid target. Prompt redeposition was also taken into account. A fluid model was adopted for the neutral species, for the sake of simplicity.

For both Li and Sn, our calculations indicate that the targets operate in a regime of *vapor shielding*, characterized by relatively strong evaporation inducing significant radiation in the proximity of the OT, with the consequent self-mitigation of the target heat load. For Li, we found that the resulting core plasma dilution is excessive, and that the peak target heat load is larger than the power handling limit of the target design considered in this work. For Sn, the core plasma contamination was computed to be tolerable only at sufficiently large values of $n_{e,sep}$, and the computed peak heat flux is again close to the power handling limit of the design considered. These results indicated that the operational window for the EU DEMO equipped with a CPS-based LMD without any additional impurity seeding is narrow, if it exists.

These results motivated us to further consider the effects of seeding Ar. The resulting increase in SOL radiation was found to successfully mitigate the heat load to the target, effectively replacing the self-mitigation offered by vapor shielding.

This led to a significant reduction of the erosion rate for both Li and Sn, noticeably widening the operational window in terms of core plasma compatibility, and to a reduction in the peak target heat flux, allowing to comply with the heat handling limits of the LMD designs here considered. This suggests that an LMD can be operated in a plasma scenario similar to the one of a solid divertor in terms of e.g. high recycling and impurity seeding. At the same time, an LMD would still be more resilient to off-normal events with respect to a solid divertor, thanks to the target self-protection (via vapor shielding) and self-replenishment (via capillary forces).

In the future, we plan to include a more accurate kinetic model for the neutrals, to better describe their behavior. This will also allow to assess the effectiveness of increasing the divertor closure in reducing the metal migration towards the core plasma – moving towards a "vapor-box" divertor [62]. This strategy, which is foreseen to be interesting mostly for Li, could significantly improve the performance for the D+Li case, even though design integration issues would be more severe. We also plan to perform a more systematic assessment of the compatibility of the impurity flux entering the separatrix with the plasma operation (e.g. by coupling SOLPS-ITER to ASTRA, see [63,64]) and to validate the erosion model, e.g. relying on experiments in linear plasma devices [13]. It could also be of interest to extend the analysis to detached plasma regimes (which would require larger $n_{e,sep}$ and/or Γ_{Ar}).

Acknowledgments

This work has been carried out within the framework of the EUROfusion Consortium and has received funding from the Euratom research and training programme 2014–2018 and 2019-2020 under grant agreement No 633053. The views and opinions expressed herein do not necessarily reflect those of the European Commission. We thank Dr. D. Coster and Dr. M. O'Mullane for their support in retrieving atomic data for Sn.

Computational resources were partially provided by HPC@POLITO (http://www.hpc.polito.it).

Appendix 1. Data availability

The simulations reported in the present work are stored in the MDSplus database. The identification numbers (*MDSplus IDs*) of the simulations are reported in Table 2.

Table 2. MDSplus IDs of the simulations performed during the presented work.

		$n_{e,sep}$ = 3.5 · 10^{19} m^{-3}	$n_{e,sep}$ = 3.75 · 10^{19} m^{-3}	$n_{e,sep}$ = 4.0 · 10^{19} m^{-3}	$n_{e,sep}$ = 4.25 · 10^{19} m^{-3}	$n_{e,sep}$ = 4.5 · 10^{19} m^{-3}
D+Li		182286	182287	182288	182289	182290
D+Sn		182222	182223	182398	182399	182226
D+Li+Ar	$\Gamma_{Ar} = 5\cdot10^{20}$ s^{-1}	182275	182276	182277	182278	182279
	$\Gamma_{Ar} = 7\cdot10^{20}$ s^{-1}	182280	182281	182282	182283	182284
	$\Gamma_{Ar} = 1\cdot10^{21}$ s^{-1}	182270	182271	182272	182273	182274
D+Sn+Ar	$\Gamma_{Ar} = 5\cdot10^{20}$ s^{-1}	182233	182234	182235	182330	182237
	$\Gamma_{Ar} = 7\cdot10^{20}$ s^{-1}	182238	182239	182446	182241	182242
	$\Gamma_{Ar} = 1\cdot10^{21}$ s^{-1}	182444	182445	182229	182230	182231

References

[1] A.J. Donné, European Research Roadmap to the Realisation of Fusion Energy, (2018). https://www.euro-fusion.org/fileadmin/user_upload/EUROfusion/Documents/2018_Research_roadmap_long_version_01.pdf (accessed January 7, 2019).

[2] M. Li, J.H. You, Interpretation of the deep cracking phenomenon of tungsten monoblock targets observed in high-heat-flux fatigue tests at 20 MW/m2, Fusion Eng. Des. 101 (2015) 1–8. https://doi.org/10.1016/j.fusengdes.2015.09.008.

[3] R.P. Wenninger, M. Bernert, T. Eich, E. Fable, G. Federici, A. Kallenbach, A. Loarte, C. Lowry, D. McDonald, R. Neu, T. Pütterich, P. Schneider, B. Sieglin, G. Strohmayer, F. Reimold, M. Wischmeier, DEMO divertor limitations during and in between ELMs, Nucl. Fusion. 54 (2014) 114003 (8pp). https://doi.org/10.1088/0029-5515/54/11/114003.

[4] R.E. Nygren, F.L. Tabarés, Liquid surfaces for fusion plasma facing components—A critical review. Part I: Physics and PSI, Nucl. Mater. Energy. 9 (2016) 6–21. https://doi.org/10.1016/j.nme.2016.08.008.

[5] C.E. Kessel, D. Andruczyk, J.P. Blanchard, T. Bohm, A. Davis, K. Hollis, P.W. Humrickhouse, M. Hvasta, M. Jaworski, J. Jun, Y. Katoh, A. Khodak, J. Klein, E. Kolemen, G. Larsen, R. Majeski, B.J. Merrill, N.B. Morley, G.H. Neilson, B. Pint, M.E. Rensink, T.D. Rognlien, A.F. Rowcliffe, S. Smolentsev, M.S. Tillack, L.M. Waganer, G.M. Wallace, P. Wilson, S.-J. Yoon, Critical Exploration of Liquid Metal Plasma-Facing Components in a Fusion Nuclear Science Facility, Fusion Sci. Technol. 75 (2019) 886–917.

https://doi.org/10.1080/15361055.2019.1610685.

[6] S. V Mirnov, V.A. Evtikhin, The tests of liquid metals (Ga, Li) as plasma facing components in T-3M and T-11M tokamaks, Fusion Eng. Des. 81 (2006) 113–119. https://doi.org/10.1016/j.fusengdes.2005.10.003.

[7] G. Mazzitelli, M.L. Apicella, G. Apruzzese, F. Crescenzi, F. Iannone, G. Maddaluno, V. Pericoli-Ridolfini, S. Roccella, M. Reale, B. Viola, I. Lyublinski, A. Vertkov, Experiments on FTU with an actively water cooled liquid lithium limiter, J. Nucl. Mater. 463 (2015) 1152–1155. https://doi.org/10.1016/j.jnucmat.2014.12.050.

[8] G. Mazzitelli, M.L. Apicella, M. Iafrati, G. Apruzzese, F. Bombarda, F. Crescenzi, L. Gabellieri, A. Mancini, M. Marinucci, A. Romano, Experiments on the Frascati Tokamak Upgrade with a liquid tin limiter, Nucl. Fusion. 59 (2019) 096004 (8pp). https://doi.org/10.1088/1741-4326/ab1d70.

[9] T.W. Morgan, A. Vertkov, K. Bystrov, I. Lyublinski, J.W. Genuit, G. Mazzitelli, Power handling of a liquid-metal based CPS structure under high steady-state heat and particle fluxes, Nucl. Mater. Energy. 12 (2017) 210–215. https://doi.org/10.1016/j.nme.2017.01.017.

[10] V.A. Evtikhin, I.E. Lyublinski, A. V. Vertkov, S. V. Mirnov, V.B. Lazarev, N.P. Petrova, S.M. Sotnikov, A.P. Chernobai, B.I. Khripunov, V.B. Petrov, D.Y. Prokhorov, V.M. Korzhavin, Lithium divertor concept and results of supporting experiments, Plasma Phys. Control. Fusion. 44 (2002) 955–977. https://doi.org/10.1088/0741-3335/44/6/322.

[11] G.G. Van Eden, V. Kvon, M.C.M. Van De Sanden, T.W. Morgan, Oscillatory vapour shielding of liquid metal walls in nuclear fusion devices, Nat. Commun. 8 (2017) 192 (10pp). https://doi.org/10.1038/s41467-017-00288-y.

[12] A. V. Vertkov, A. V. Voronin, V.K. Gusev, E. V. Demina, I.E. Lyublinskiy, V.N. Pimenov, M.D. Prusakova, Behavior of Capillary-Porous Systems with Liquid Lithium under Influence of Pulsed Deuterium Plasma, Inorg. Mater. Appl. Res. 10 (2019) 326–332. https://doi.org/10.1134/S2075113319020382.

[13] T.W. Morgan, P. Rindt, G.G. Van Eden, V. Kvon, M.A. Jaworksi, N.J.L. Cardozo, Liquid metals as a divertor plasma-facing material explored using the Pilot-PSI and Magnum-PSI linear devices, Plasma Phys. Control. Fusion. 60 (2018) 14025 (11 pp). https://doi.org/10.1088/1361-6587/aa86cd.

[14] G.F. Nallo, G. Mazzitelli, L. Savoldi, F. Subba, R. Zanino, Self-consistent modelling of a liquid metal box-type divertor with application to the divertor tokamak test facility: Li versus Sn, Nucl. Fusion. 59 (2019) 066020 (17pp). https://doi.org/10.1088/1741-4326/ab145b.

[15] G.G. Van Eden, T.W. Morgan, D.U.B.B. Aussems, M.A. Van Den Berg, K. Bystrov, M.C.M.M. Van De Sanden, Self-Regulated Plasma Heat Flux Mitigation Due to Liquid Sn Vapor Shielding, Phys. Rev. Lett. 116 (2016) 1–5. https://doi.org/10.1103/PhysRevLett.116.135002.

[16] P. Rindt, T.W. Morgan, G.G. Van Eden, M.A. Jaworski, N.J. Lopes Cardozo, Power handling and vapor shielding of pre-filled lithium divertor targets in Magnum-PSI, Nucl. Fusion. 59 (2019) 056003 (13pp). https://doi.org/10.1088/1741-4326/ab0560.

[17] A. Vertkov, I. Lyublinski, M. Zharkov, A. Berlov, S. Mirnov, A. Komov, A. Zakharenkov, The concept of lithium based plasma facing elements for steady state fusion tokamak-reactor and its experimental validation, in: 2018 IAEA Fusion Energy Conf. - EX/P1-12, Gandhinagar, 2018. https://nucleus.iaea.org/sites/fusionportal/Shared Documents/FEC 2018/FEC2018_ConfMat_Online.pdf (accessed January 7, 2019).

[18] S. Roccella, G. Dose, R. de Luca, M. Iafrati, A. Mancini, G. Mazzitelli, CPS Based Liquid Metal Divertor Target for EU-DEMO, J. Fusion Energy. (2020) (7pp). https://doi.org/10.1007/s10894-020-00263-4.

[19] P. Rindt, T.W. Morgan, M.A. Jaworski, N.J. Lopes Cardozo, Power handling limit of liquid lithium divertor targets, Nucl. Fusion. 58 (2018) 104002 (5pp). https://doi.org/10.1088/1741-4326/aad290.

[20] F. Subba, L. Aho-Mantila, D. Coster, G. Maddaluno, G.F. Nallo, B. Sieglin, R. Wenninger, R. Zanino, Modelling of mitigation of the power divertor loading for the EU DEMO through Ar injection, Plasma Phys. Control. Fusion. 60 (2018) 035013 (9pp). https://doi.org/10.1088/1361-6587/aaa508.

[21] R.J. Goldston, M.L. Reinke, J.A. Schwartz, A new scaling for divertor detachment, Plasma Phys. Control. Fusion. 59 (2017) 055015 (7pp). https://doi.org/10.1088/1361-6587/aa5e6e.

[22] G.F. Nallo, S. Carli, G. Caruso, F. Crisanti, G. Mazzitelli, L. Savoldi, F. Subba, R. Zanino, Modeling the lithium loop in a liquid metal pool-type divertor, Fusion Eng. Des. 125 (2017) 206–215. https://doi.org/10.1016/j.fusengdes.2017.07.004.

[23] E.D. Marenkov, A.A. Pshenov, Vapor shielding of liquid lithium divertor target during steady-state and transient events, Nucl. Fus. 60 (2020) 026011 (12pp). https://doi.org/https://doi.org/10.1088/1741-4326/ab5eb5.

[24] M.E. Rensink, T.D. Rognlien, C.E. Kessel, Modeling the Edge-Plasma Interface for Liquid-Lithium Walls in FNSF, Fusion Sci. Technol. 75 (2019) 959–972. https://doi.org/10.1080/15361055.2019.1643686.

[25] E.D. Marenkov, A.S. Kukushkin, A.A. Pshenov, Modeling the vapor shielding of a liquid lithium divertor target using SOLPS 4.3 code, Nucl. Fusion. 61 (2021) 034001 (7pp). https://doi.org/10.1088/1741-4326/abd642.

[26] E.D. Emdee, R.J. Goldston, J.D. Lore, X. Zhang, Predictive modeling of a lithium vapor box divertor in NSTX-U using SOLPS-ITER, Nucl. Mater. Energy. 27 (2021) 101004 (6pp). https://doi.org/10.1016/j.nme.2021.101004.

[27] V. Pericoli Ridolfini, R. Ambrosino, S. Mastrostefano, P. Chmielewski, M. Poradziński, R. Zagórski, M. Poradzinski, R. Zagorski, A comparative study of the effects of liquid lithium and tin as DEMO divertor targets

on the heat loads and SOL properties, Phys. Plasmas. 26 (2019) 12507 (13pp). https://doi.org/10.1063/1.5055017.

[28] V. Pericoli Ridolfini, R. Ambrosino, P. Chmielewski, F. Crisanti, M. Poradziński, R. Zagorski, Perspectives for the Liquid Lithium and Tin Targets in the I-DTT Divertor, Nucl. Fusion. 59 (2019) 126008 (15pp). https://doi.org/10.1088/1741-4326/ab3969.

[29] M. Poradziński, I. Ivanova-Stanik, G. Pełka, R. Zagórski, Integrated core-SOL-divertor modelling for DEMO with tin divertor, Fusion Eng. Des. 124 (2017) 248–251. https://doi.org/10.1016/j.fusengdes.2017.04.131.

[30] A. V Vertkov, I.E. Lyublinski, M.Y. Zharkov, In-Vessel Devices Based on Capillary-Porous Systems with Liquid Metal for a Stationary Tokamak, Plasma Phys. Reports. 44 (2018) 664–670. https://doi.org/10.1134/S1063780X18070073.

[31] J.P. Allain, M.D. Coventry, D.N. Ruzic, Collisional and thermal effects on liquid lithium sputtering, Phys. Rev. B - Condens. Matter Mater. Phys. 76 (2007) 205434 (12pp). https://doi.org/10.1103/PhysRevB.76.205434.

[32] T. Abrams, M.A. Jaworski, M. Chen, E.A. Carter, R. Kaita, D.P. Stotler, G. De Temmerman, T.W. Morgan, M.A. Van Den Berg, H.J. Van Der Meiden, Suppressed gross erosion of high-temperature lithium via rapid deuterium implantation, Nucl. Fusion. 56 (2016) 16022 (10pp). https://doi.org/10.1088/0029-5515/56/1/016022.

[33] J.P. Allain, J.N. Brooks, Lithium surface-response modelling for the NSTX liquid lithium divertor, Nucl. Fusion. 51 (2011) 023002 (8pp). https://doi.org/10.1088/0029-5515/51/2/023002.

[34] T. Abrams, Erosion and re-deposition of Lithium and Boron coatings under high-flux plasma bombardment, Ph.D. thesis, Princeton University, 2015. http://arks.princeton.edu/ark:/88435/dsp01jm214r372.

[35] J.P.S. Loureiro, H. Fernandes, F.L. Tabarés, G. Mazzitelli, C. Silva, R. Gomes, E. Alves, R. Mateus, T. Pereira, H. Figueiredo, H. Alves, Deuterium retention in tin (Sn) and lithium–tin (Li–Sn) samples exposed to ISTTOK plasmas, Nucl. Mater. Energy. 12 (2017) 709–713. https://doi.org/10.1016/j.nme.2016.12.026.

[36] J.P. Allain, C.N. Taylor, Lithium-based surfaces controlling fusion plasma behavior at the plasma-material interface, Phys. Plasmas. 19 (2012) 56126 (9pp). https://doi.org/10.1063/1.4719688.

[37] G. Mazzitelli, M.L. Apicella, M. Iafrati, G. Apruzzese, F. Bombarda, F. Crescenzi, L. Gabellieri, A. Mancini, M. Marinucci, A. Romano, Experiments on the Frascati Tokamak Upgrade with a liquid tin limiter, Nucl. Fusion. 59 (2019) 096004 (8pp). https://doi.org/10.1088/1741-4326/ab1d70.

[38] S. Wiesen, D. Reiter, V. Kotov, M. Baelmans, W. Dekeyser, A.S. Kukushkin, S.W. Lisgo, R.A. Pitts, V. Rozhansky, G. Saibene, I. Veselova, S. Voskoboynikov, The new SOLPS-ITER code package, J. Nucl. Mater. 463 (2015) 480–484. https://doi.org/10.1016/j.jnucmat.2014.10.012.

[39] D.P. Coster, Reduced Physics Models in SOLPS for Reactor Scoping Studies, Contrib. to Plasma Phys. 56 (2016) 790–795. https://doi.org/10.1002/ctpp.201610035.

[40] M. Blommaert, N. Horsten, P. Börner, W. Dekeyser, A spatially hybrid fluid-kinetic neutral model for SOLPS-ITER plasma edge simulations, Nucl. Mater. Energy. 19 (2019) 28–33. https://doi.org/10.1016/j.nme.2019.01.022.

[41] E. Sytova, E. Kaveeva, V. Rozhansky, I. Senichenkov, S. Voskoboynikov, D. Coster, X. Bonnin, R.A. Pitts, Impact of a new general form of friction and thermal forces on SOLPS-ITER modelling results, Contrib. to Plasma Phys. 58 (2018) 622–628. https://doi.org/10.1002/ctpp.201700135.

[42] F. Subba, SOLPS Calculations for DEMO, EUROfusion report EFDA_D_2N3L2S, 2020.

[43] H.P. Summers, The ADAS User Manual, version 2.6, 2004. http://www.adas.ac.uk/man/contents.pdf (accessed January 7, 2019).

[44] D. Coster, M. O'Mullane, Private communication, (2019).

[45] E. Kaveeva, V. Rozhansky, I. Senichenkov, E. Sytova, I. Veselova, S. Voskoboynikov, X. Bonnin, R.A. Pitts, A.S. Kukushkin, S. Wiesen, D. Coster, SOLPS-ITER modelling of ITER edge plasma with drifts and currents, Nucl. Fusion. 60 (2020) 046019 (14pp). https://doi.org/10.1088/1741-4326/ab73c1.

[46] A.W. Leonard, Plasma detachment in divertor tokamaks, Plasma Phys. Control. Fusion. 60 (2018) 04401 (24pp). https://doi.org/10.1088/1361-6587/aaa7a9.

[47] Y.R. Martin, T. Takizuka, Power requirement for accessing the H-mode in ITER, J. Phys. Conf. Ser. 123 (2008) 012033 (11pp). https://doi.org/10.1088/1742-6596/123/1/012033.

[48] T.W. Morgan, P. Rindt, G.G. Van Eden, V. Kvon, M.A. Jaworksi, N.J. Lopes Cardozo, Liquid metals as a divertor plasma facing material explored using the Pilot-PSI and Magnum- PSI linear devices, Plasma Phys. Control. Fusion. 60 (2018) 014025 (11pp). https://doi.org/10.1088/1361-6587/aa86cd.

[49] S. Carli, R.A. Pitts, X. Bonnin, F. Subba, R. Zanino, Effect of strike point displacements on the ITER tungsten divertor heat loads, Nucl. Fusion. 58 (2018) 126022 (21pp). https://doi.org/10.1088/1741-4326/aae43f.

[50] M. Warrier, R. Schneider, X. Bonnin, Subroutines for some plasma surface interaction processes: Physical sputtering, chemical erosion, radiation enhanced sublimation, backscattering and thermal evaporation, Comput. Phys. Commun. 160 (2004) 46–68. https://doi.org/10.1016/j.cpc.2004.02.011.

[51] V. Pericoli Ridolfini, Final Report on Deliverable DTT1-LMD.P2-T003, EUROfusion report EFDA_D_2NJWW3, 2020.

[52] J. Safarian, T.A. Engh, Vacuum Evaporation of Pure Metals, Metall. Mater. Trans. A. 44 (2013) 747–753. https://doi.org/10.1007/s11661-012-1464-2.

[53] M. Iafrati, Phenomenology of plasma-wall interaction using liquid metals in tokamak devices, Ph.D. thesis,

Università degli studi di Padova, 2018. http://paduaresearch.cab.unipd.it/11904/.

[54] A. V. Chankin, D.P. Coster, R. Dux, Monte Carlo simulations of tungsten redeposition at the divertor target, Plasma Phys. Control. Fusion. 56 (2014) 025003 (11pp). https://doi.org/10.1088/0741-3335/56/2/025003.

[55] P.C. Stangeby, The Plasma Boundary of Magnetic Fusion Devices, Institute of Physics Publishing, London, 2001. https://doi.org/10.1088/0741-3335/43/2/702.

[56] V. Pericoli Ridolfini, P. Chmielewski, I. Ivanova-Stanik, M. Poradziński, R. Zagórski, R. Ambrosino, F. Crisanti, Comparison between liquid lithium and liquid tin targets in reactor relevant conditions for DEMO and I-DTT, Phys. Plasmas. 27 (2020) 112506 (11pp). https://doi.org/10.1063/5.0012743.

[57] M. Carr, A. Meakins, A. Baciero, C. Giroud, CHERAB's documentation, (2018). https://cherab.github.io/documentation/index.html.

[58] M. Carr, A. Meakins, cherab/core: Release v1.1.0, (2019). https://doi.org/10.5281/zenodo.2585962.

[59] M. Moscheni, M. Carr, S. Dulla, F. Maviglia, A. Meakins, G.F. Nallo, F. Subba, R. Zanino, Radiative Heat Load Distribution on the EU-DEMO First Wall Due to Mitigated Disruptions, Nucl. Mater. Energy. 25 (2020) 100824 (6pp). https://doi.org/https://doi.org/10.1016/j.nme.2020.100824.

[60] M. Moscheni, M. Carr, S. Dulla, F. Maviglia, A. Meakins, G.F. Nallo, F. Subba, R. Zanino, Parametric study of the radiative load distribution in the EU-DEMO first wall due to SPI-mitigated disruptions, submitted to Fusion Engineering and Design, (2021).

[61] T. Pütterich, E. Fable, R. Dux, M. O'Mullane, R. Neu, M. Siccinio, Determination of the tolerable impurity concentrations in a fusion reactor using a consistent set of cooling factors, Nucl. Fusion. 59 (2019) 056013 (28pp). https://doi.org/10.1088/1741-4326/ab0384.

[62] R.J. Goldston, R. Myers, J. Schwartz, The lithium vapor box divertor, Phys. Scr. T167 (2016) 14017 (6pp). https://doi.org/10.1088/0031-8949/T167/1/014017.

[63] I.Y. Senichenkov, E.G. Kaveeva, V.A. Rozhansky, S.P. Voskoboynikov, P.A. Molchanov, D.P. Coster, G. V. Pereverzev, Integrated modeling of H-mode tokamak discharges with ASTRA and B2SOLPS numerical codes, Plasma Phys. Control. Fusion. 56 (2014) 055002 (12pp). https://doi.org/10.1088/0741-3335/56/5/055002.

[64] I.Y. Senichenkov, E.G. Kaveeva, A. V. Gogoleva, E.O. Vekshina, G. V. Zadvitskiy, P.A. Molchanov, V.A. Rozhansky, S.P. Voskoboynikov, N.A. Khromov, S.A. Lepikhov, V.K. Gusev, Integrated modelling of the Globus-M tokamak plasma and a comparison with SOL width scaling, Nucl. Fusion. 55 (2015) 053012 (7pp). https://doi.org/10.1088/0029-5515/55/5/053012.